

UNCLASSIFIED

Defense Technical Information Center
Compilation Part Notice

ADP012091

TITLE: Supercavitating 3-D Hydrofoils and Propellers: Prediction of Performance and Design

DISTRIBUTION: Approved for public release, distribution unlimited

This paper is part of the following report:

TITLE: Supercavitating Flows [les Ecoulements supercavitants]

To order the complete compilation report, use: ADA400728

The component part is provided here to allow users access to individually authored sections of proceedings, annals, symposia, etc. However, the component should be considered within the context of the overall compilation report and not as a stand-alone technical report.

The following component part numbers comprise the compilation report:
ADP012072 thru ADP012091

UNCLASSIFIED

SUPERCAVITATING 3-D HYDROFOILS AND PROPELLERS: PREDICTION OF PERFORMANCE AND DESIGN

Spyros A. Kinnas

Ocean Engineering Group, Department of Civil Engineering
The University of Texas at Austin, Austin, TX 78712, USA
http://cavity.ce.utexas.edu, email: kinnas@mail.utexas.edu

ABSTRACT

Recent numerical techniques for the prediction of cavitating flows, in linear and non-linear theories, are applied on super-cavitating 2-D, 3-D hydrofoils and propellers. Some of these techniques, when incorporated within a non-linear optimization algorithm, can lead to efficient supercavitating hydrofoil or propeller designs. This lecture will address 3-D supercavitating hydrofoils, supercavitating and surface-piercing propellers.¹²

NOMENCLATURE

α	Angle Of Attack For 3-D Hydrofoil
C_p	Pressure Coefficient, $C_p = (P - P_o)/(\frac{\rho}{2}n^2D^2)$
D	Propeller Diameter
η	Propeller efficiency, $\eta = \frac{K_T}{K_Q} \frac{J_S}{2\pi}$
F_r	Froude Number, $F_r = n^2D/g$
g	Gravitational Acceleration
Γ	Circulation Around Each Blade Section
h	Cavity Thickness Over The Blade Surface
h_w	Cavity Thickness Over The Wake Surface
J_S	Advance Ratio, $J_S = V_s/nD$
K_Q	Torque Coefficient, $K_Q = Q/\rho n^2D^5$
K_T	Thrust Coefficient, $K_T = T/\rho n^2D^4$
l	Cavity Length
n	Propeller Rotational Frequency (rev/s)
\vec{n}	Unit Normal Vector
ϕ	Perturbation Potential
P	Pressure
P_o	Pressure Far Upstream, at the Propeller Axis
P_v	Vapor Pressure of Water
P_∞	Pressure Far Upstream, at the Submergence Depth of the Hydrofoil
\vec{q}	Total Velocity
\vec{q}_{in}	Local Inflow Velocity (with respect to propeller-fixed coordinates system)
\vec{q}_{wake}	Effective Wake Inflow Velocity (with respect to ship-fixed coordinates system)
Q	Propeller Torque
ρ	Fluid Density
σ	Cavitation Number Based on U_∞ , $\sigma = (P_\infty - P_v)/(\frac{\rho}{2}U_\infty^2)$
σ_n	Cavitation Number Based on n , $\sigma_n = (P_o - P_v)/(\frac{\rho}{2}n^2D^2)$
σ_v	Cavitation Number based on V_s , $\sigma_v = (P_o - P_v)/(\frac{\rho}{2}V_s^2)$
t	Time
T	Propeller Thrust
U_∞	Speed of Uniform Inflow for Hydrofoils
V_s	Ship Speed

¹²Sections, figures, equations and footnotes are numbered starting from the first lecture of Prof. Kinnas.

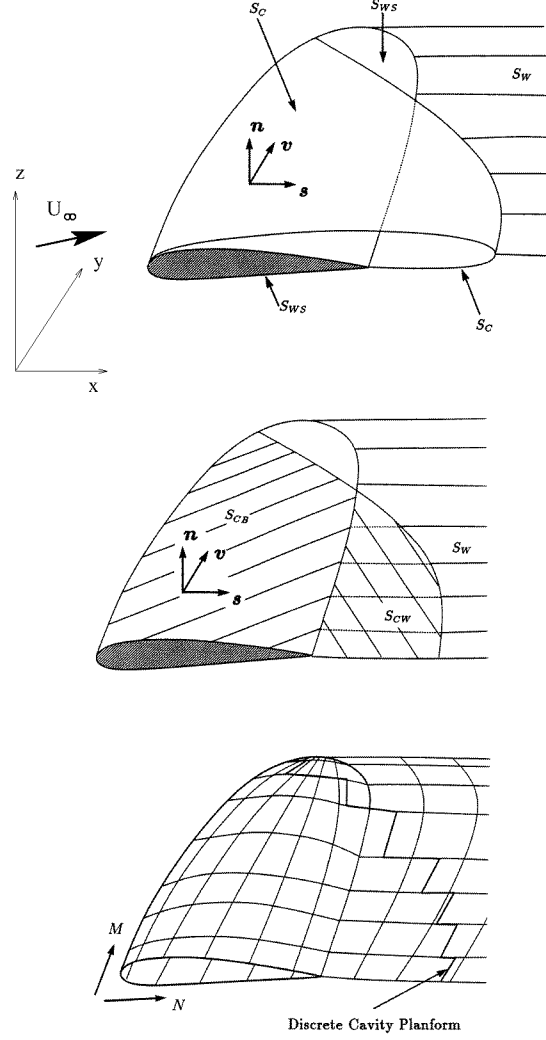


Figure 23: Definition of the “exact”, the approximate, and the discretized 3-D cavity and foil surface.

4 3-D HYDROFOIL

4.1 Formulation

Consider now a 3-D hydrofoil which is subject to a uniform inflow \mathbf{U}_∞ as shown in Fig. 23. The cavity surface is denoted with S_C , the wetted hydrofoil surface with S_{WS} , and the trailing wake surface with S_W . The total flow velocity field $\mathbf{q}(x, y, z)$, can be written in terms of the perturbation potential, $\phi(x, y, z)$, as follows:

$$\mathbf{q}(x, y, z) = \mathbf{U}_\infty + \nabla \phi(x, y, z). \quad (81)$$

In the next four sections the necessary equations and conditions for determining $\phi(x, y, z)$, as well as the cavity planform and shape are outlined. Only the non-linear cavity solution is described. References on linearized approaches have been given in the introduction.

4.1.1 The Green's formula

As in the case of the 2-D hydrofoil Green's third identity renders the following integral equation for $\phi(x, y, z)$:

$$\begin{aligned}
2\pi\phi &= \int_{S_{WS} \cup S_C} \left[\phi \frac{\partial G}{\partial n} - G \frac{\partial \phi}{\partial n} \right] dS \\
&+ \int_{S_W} \Delta\phi_W \frac{\partial G}{\partial n} dS
\end{aligned} \tag{82}$$

\mathbf{n} is the unit vector normal to the foil wetted surface, the cavity surface or the wake surface; $\Delta\phi$ is the potential jump across the wake sheet; $G = 1/R$ is the Green's function, where R is the distance between a point P and the point of integration along the foil and cavity surface.

Equation (82) should be applied on the “exact” cavity surface as shown in Fig. 23. Based on the fast convergence of the boundary element method with number of iterations in 2-D (as described in the previous section), only the solution from the hybrid scheme (i.e. the first iteration) is carried out. This is equivalent to applying Green's formula on an approximate surface, as shown in Fig. 23. This surface is comprised from the foil surface and the trailing wake surface. The treatment of a supercavity within this scheme is discussed in detail in (Fine & Kinnas 1993b). The approximate surface is discretized as shown at the bottom part of Fig. 23. Constant strength dipoles and sources are distributed on each of the wetted or cavitating flow quadrilateral panels. The strength of the source distribution on the wetted foil surface is expressed via the kinematic boundary condition:

$$\frac{\partial \phi}{\partial n} = -\mathbf{U}_\infty \cdot \mathbf{n}; \text{ on } S_{WS} \tag{83}$$

In the case of super-cavitation the cavity in the wake is modeled with constant strength line sources. Equation (82) is then split into two different formulations, on the part of the cavity over the foil, and on the part downstream of the trailing edge. The corresponding formulas are given in (Fine & Kinnas 1993a), and are similar to those given in equations (49) and (50).

4.1.2 The dynamic boundary condition

The dynamic boundary condition (DBC) requires that the pressure everywhere inside and on the cavity be constant and equal to the known cavity pressure, P_v . As in the case of 2-D hydrofoil, Bernoulli's equation will give:

$$q_c = U_\infty \sqrt{1 + \sigma} \tag{84}$$

Where q_c is the magnitude of the cavity velocity \mathbf{q}_c . Note that for simplicity the hydrostatic terms, which would be important in the case of a vertical 3-D foil, have not been included.

The cavity velocity vector, \mathbf{q}_c , may also be expressed as follows (Kinnas & Fine 1993):

$$\mathbf{q}_c = \frac{V_s [\mathbf{s} - (\mathbf{s} \cdot \mathbf{v})\mathbf{v}] + V_v [\mathbf{v} - (\mathbf{s} \cdot \mathbf{v})\mathbf{s}]}{\|\mathbf{s} \times \mathbf{v}\|^2} \tag{85}$$

where s and v are the curvilinear coordinates¹³ along the cavity surface (as shown in Fig. 23); \mathbf{s} and \mathbf{v} are the corresponding unit vectors; V_s and V_v are given as follows:

$$V_s = \frac{\partial \phi}{\partial s} + \mathbf{U}_\infty \cdot \mathbf{s}; \quad V_v = \frac{\partial \phi}{\partial v} + \mathbf{U}_\infty \cdot \mathbf{v} \tag{86}$$

Equations (84) and (85) may then be combined to form an equation which is quadratic in the unknown chordwise perturbation velocity, $\partial\phi/\partial s$. The solution to this quadratic¹⁴ renders $\partial\phi/\partial s$ in terms of the cavitation number, the inflow velocity, and the unknown crossflow $\partial\phi/\partial v$:

$$\frac{\partial \phi}{\partial s} = -\mathbf{U}_\infty \cdot \mathbf{s} + V_v \cos \theta + \sin \theta \sqrt{q_c^2 - V_v^2} \tag{87}$$

with θ being the angle between s and v ; q_c is given by equation (84). Equation (87) is integrated once to form a Dirichlet boundary condition on ϕ :

¹³In general non-orthogonal.

¹⁴The root which corresponds to cavity velocity vectors pointing downstream is selected.

$$\phi(s) = \phi(0) + \int_0^s [\text{right-hand-side of equ. (87)}] ds \quad (88)$$

The value of $\phi(0)$ in equation (88) at each strip is determined (as in the case of 2-D hydrofoil) via a cubic extrapolation in terms of the unknown potentials on the wetted panels on the same strip in front of the cavity.

The crossflow term, $\partial\phi/\partial v$, in equation (88) is included in an iterative sense (Kinnas & Fine 1993).

4.1.3 The cavity thickness distribution

The kinematic boundary condition on the cavity requires that the velocity normal to the cavity is zero (in the case of steady flows), or, more generally (also valid in the case of unsteady flows), that the following substantial derivative is zero:

$$\frac{D}{Dt}(n - h) = \left(\frac{\partial}{\partial t} + \mathbf{q}_c \cdot \nabla \right) (n - h) = 0 \quad (89)$$

where n is the coordinate normal to the foil surface under the cavity (with unit vector \mathbf{n}) and $h(s, v, t)$ is the thickness of the cavity normal to the foil surface at the point (s, v) at time t . Expressing the gradient in terms of the local directional derivatives

$$\nabla = \frac{[\mathbf{s} - (\mathbf{s} \cdot \mathbf{v})\mathbf{v}]}{\|\mathbf{s} \times \mathbf{v}\|^2} \frac{\partial}{\partial s} + \frac{[\mathbf{v} - (\mathbf{s} \cdot \mathbf{v})\mathbf{s}]}{\|\mathbf{s} \times \mathbf{v}\|^2} \frac{\partial}{\partial v} + \mathbf{n} \frac{\partial}{\partial n}, \quad (90)$$

and performing the dot product with \mathbf{q}_c (as defined in (85)) and finally substituting the result in (89) yields the following partial differential equation for the cavity thickness:

$$\begin{aligned} \frac{\partial h}{\partial s} [V_s - \cos \theta V_v] + \frac{\partial h}{\partial v} [V_v - \cos \theta V_s] = \\ = \sin^2 \theta (V_n - \frac{\partial h}{\partial t}) \end{aligned} \quad (91)$$

where

$$V_n = \frac{\partial \phi}{\partial n} + \mathbf{U}_\infty \cdot \mathbf{n} \quad (92)$$

The partial differential equation (91) can be integrated over the entire cavity planform in order to provide the cavity thickness. In the case of steady flow (as considered in the beginning of this section) $\partial h/\partial t = 0$. In the part of the cavity downstream of the trailing edge a different formula, similar to that given in equation (51), is used for the cavity height, h_W (Fine & Kinnas 1993a).

4.1.4 The cavity planform

The extent (planform) of the 3-D cavity is not known and has to be determined as a part of the solution. This is accomplished by finding the appropriate $l(y)$ (cavity length at each spanwise location y) which satisfies the cavity closure condition for the given cavitation number, σ :

$$\delta(y; \sigma) = h(l(y), y) = 0 \quad (93)$$

4.2 Numerical aspects

The objective of the numerical analysis is to invert equation (82) subject to the conditions (83) and (88). The numerical implementation is described in detail in (Kinnas & Fine 1991b, Kinnas & Fine 1993, Fine & Kinnas 1993a). In brief, for given cavity planform, equation (82) is solved with respect to the unknown ϕ on the wetted foil and for the unknown $\partial\phi/\partial n$ on the cavity. The cavity height at the trailing edge of the used cavity planform are then determined by integrating equation (91). The cavity planform is adjusted accordingly and the solution is carried over again until the corresponding heights at the cavity end are equal to zero within some given tolerance. The numerics of the method have been extensively validated in (Kinnas & Fine 1993, Fine & Kinnas 1993a).

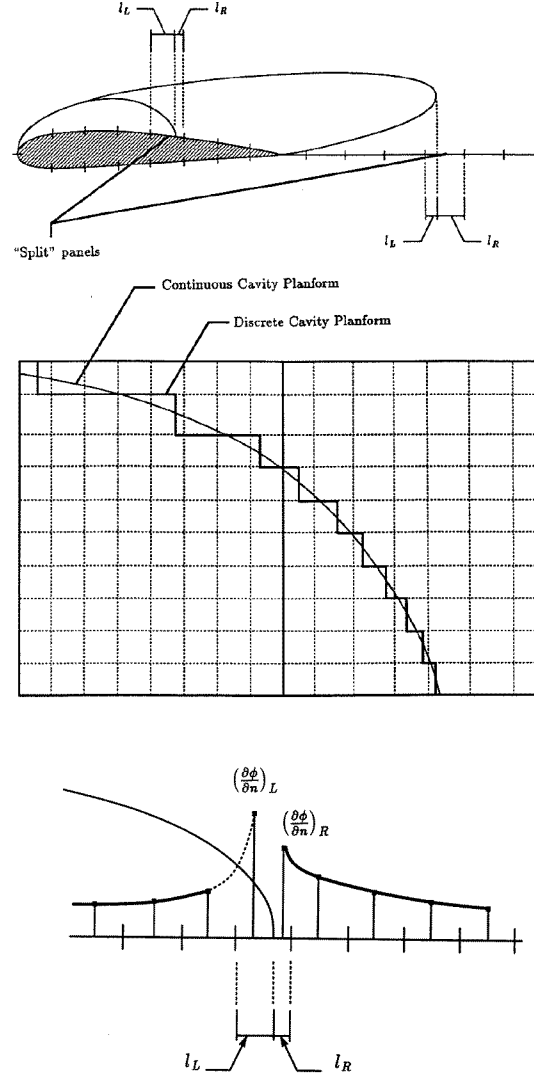


Figure 24: The split panel technique applied to the cavity trailing edge in three dimensions. The values (extrapolated from the side of the cavity) for $\partial\phi/\partial n$ into the two parts of the split panel are also shown.

4.2.1 The split panel technique

A very crucial issue in the numerical implementation was found to be related to the treatment of panels which were intersected by the cavity trailing edge. In order to avoid recomputing influence coefficients a technique was devised, namely the *split* panel technique (Kinnas & Fine 1993, Fine 1992), in which the intersected panel is treated as one panel with each of the ϕ and $\partial\phi/\partial n$ being determined as the weighted average of the values on the wetted and the cavitating part of the panel. This technique, as depicted on Fig. 24, provided substantial savings on computer time since the same panel discretization can handle arbitrary cavity planforms.

4.3 Multiplicity of Solutions

Equation (93) may accept more than one solutions, i.e. produce more than one cavity planforms for a given value of cavitation number. This is a very well known fact in two dimensions, where for some cavitation numbers there are three solutions (two partial cavities and one supercavity). The present method has also been found to predict multiple solutions in three dimensions (Kinnas & Fine 1992, Fine & Kinnas 1993a), as can be seen in Figure 25. Note that for $\sigma = 0.85$ two cavity planforms are predicted, one partial cavity and one mixed cavity (slightly supercavity at midspan). The partial cavity was produced when the initial guess was a

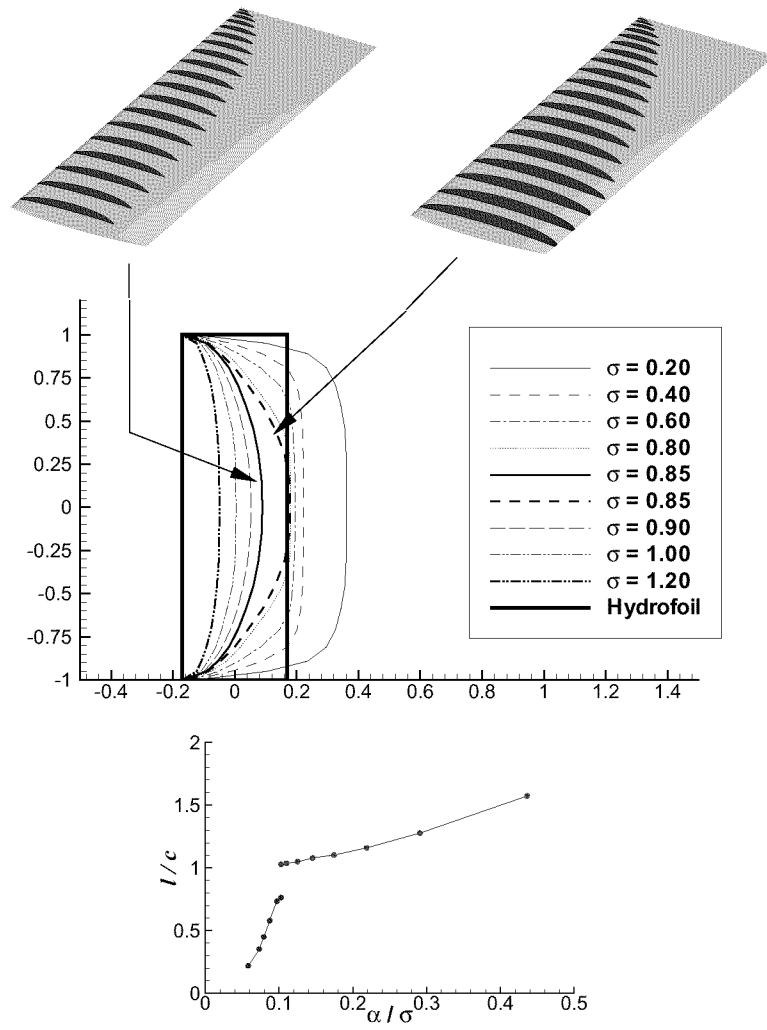


Figure 25: Multiple solutions in 3-D for $\sigma = 0.85$. The predicted cavity shapes are shown over half of the span at the top and the l_{max}/c vs. α/σ curve is shown at the bottom.

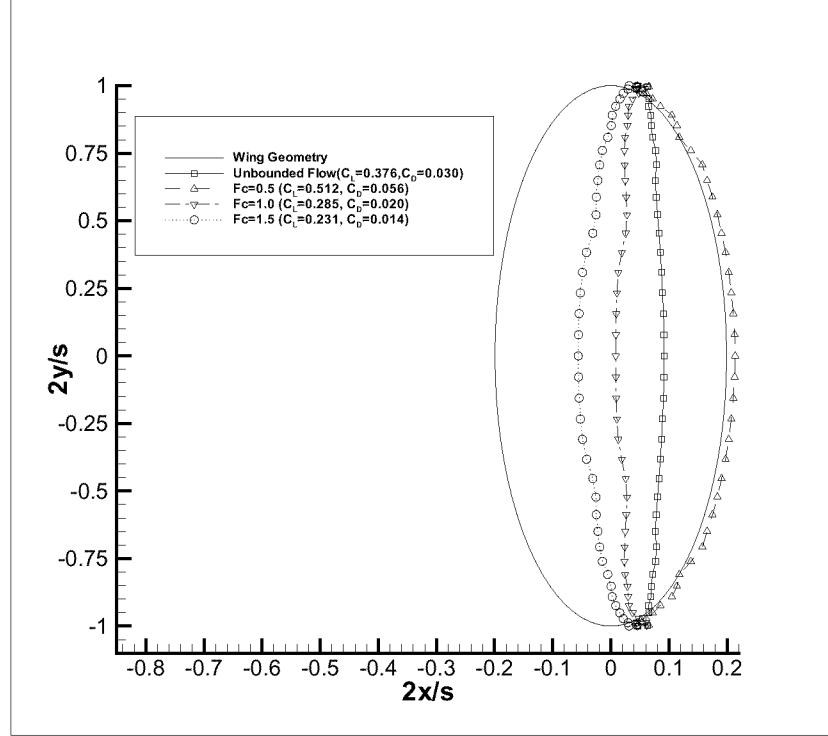


Figure 26: Froude number effect on predicted cavity planform and forces in the case the submergence depth at which the hydrofoil operates is equal to the chord length. From (Bal et al 2001).

partial cavity and the mixed cavity when the initial guess was a supercavity. The cavity length at midchord vs α/σ is also shown at the bottom part of Fig. 25. Note the striking similarity of this curve to the well known characteristic curve for a two dimensional cavitating flat plate (not shown in the Figure). This multiplicity of solutions in 3-D can also be confirmed from the observed instability on the cavity extent during experiments on cavitating 3-D foils as the cavity transitions from partial to super-cavitation.

4.4 Effects of free-surface

They are often substantial and can be evaluated by using “negative” images with respect to the free-surface in the case of very large Froude number, $F_c = U_\infty / \sqrt{gc}$, where c is the maximum chord. In the case of finite Froude numbers the free-surface must also be modeled with panels (Bal et al 2001). A representative result from applying this method is shown in Fig. 26. Notice the strong dependence of the predicted cavity planform and forces on F_c .

4.5 Effects of tunnel walls

The effects of tunnel walls are known to be substantial (especially in the prediction of cavity extent) and need to be included, either by imaging of the hydrofoil and cavity with respect to the tunnel walls (in the case of 2-D flow and square section tunnel), or by modeling completely the tunnel boundaries in the numerical method (Choi & Kinnas 1998, Choi & Kinnas 1999, Kinnas et al 1998b, Kinnas et al 2000). The paneling on the 4990 3-D hydrofoil and the tunnel walls of the DTMB 36” circular section tunnel is shown in Figure 27.

Predicted cavity shapes, with and without the tunnel effects included, are shown for the 4990 3-D hydrofoil in Figure 28. Note the drastic effect of the tunnel walls on the predicted cavity shape. The predicted cavity plan-form when the tunnel effects are included appears to be very close to the observed, shown in Figure 29. However, there are flow phenomena at the root of the blade (re-entrant jet, cloud cavitation at the trailing edge) which are not modeled in the present method and thus not captured by the predictions. The predicted cavity with the tunnel effects included, as shown in Figure 28, has been determined by manually adjusting the cavity leading edge at each section along the span until two conditions are satisfied: (a) the cavity thickness is positive and (b) the pressures upstream of the cavity detachment are larger than the vapor pressure.

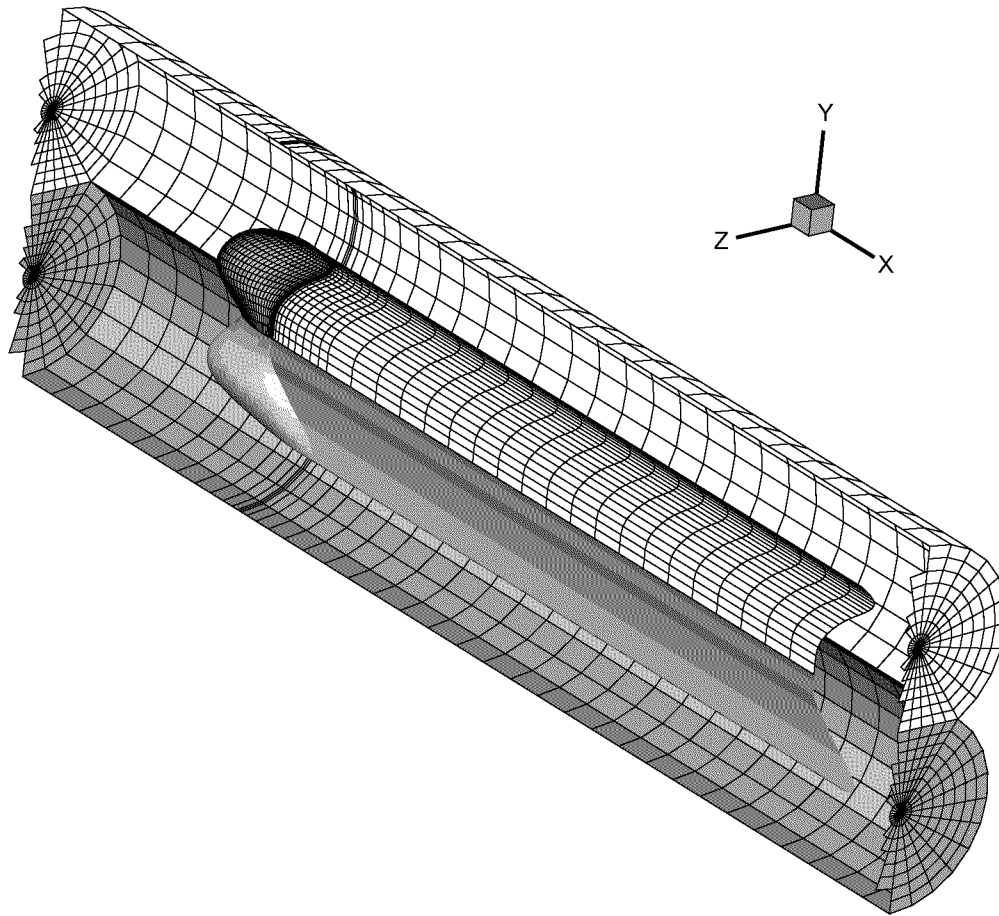


Figure 27: The grid on the 4990 hydrofoil, its trailing wake, and the DTMB 36" circular tunnel (the images with respect to the flat bottom of the tunnel are also shown). The flow goes from left to right. Only half of the tunnel panels are displayed.

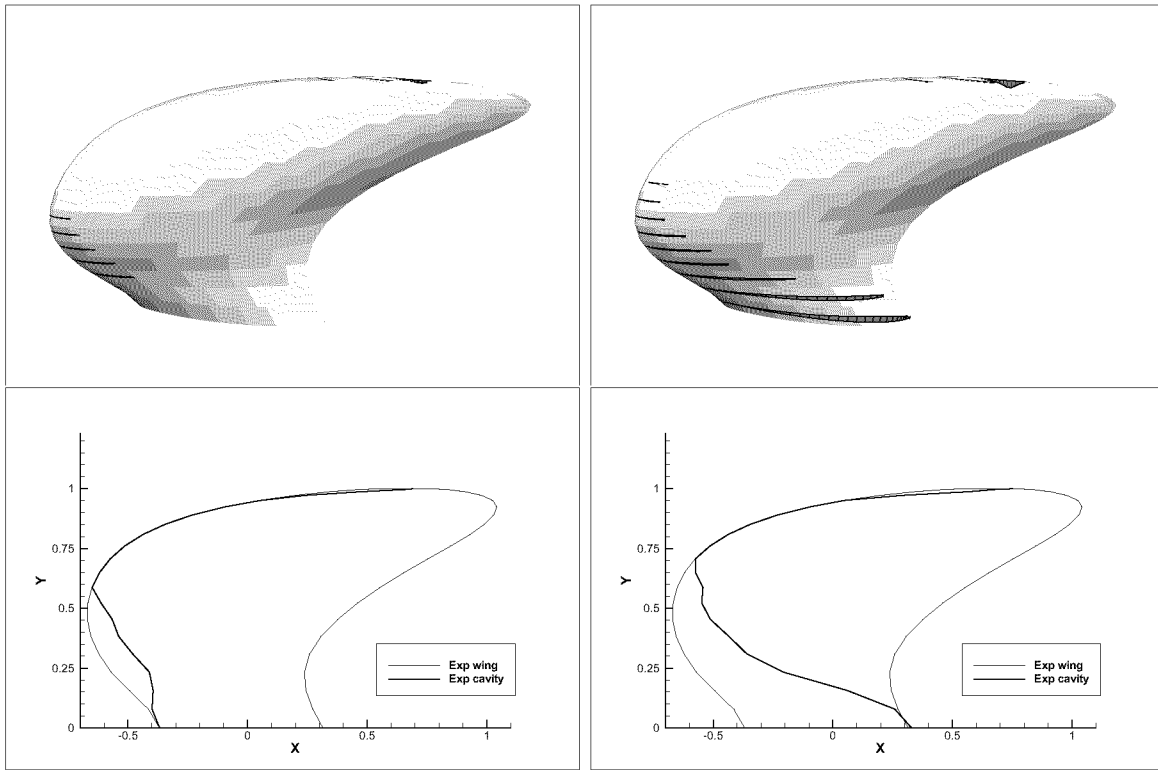


Figure 28: The predicted perspective (top) and expanded (bottom) cavity plan-forms *without* (left) and *with* (right) the tunnel wall effects for the 4990 hydrofoil; $\alpha = 0^\circ$, $\sigma = 0.62$. From (Kinnas et al 1998b).

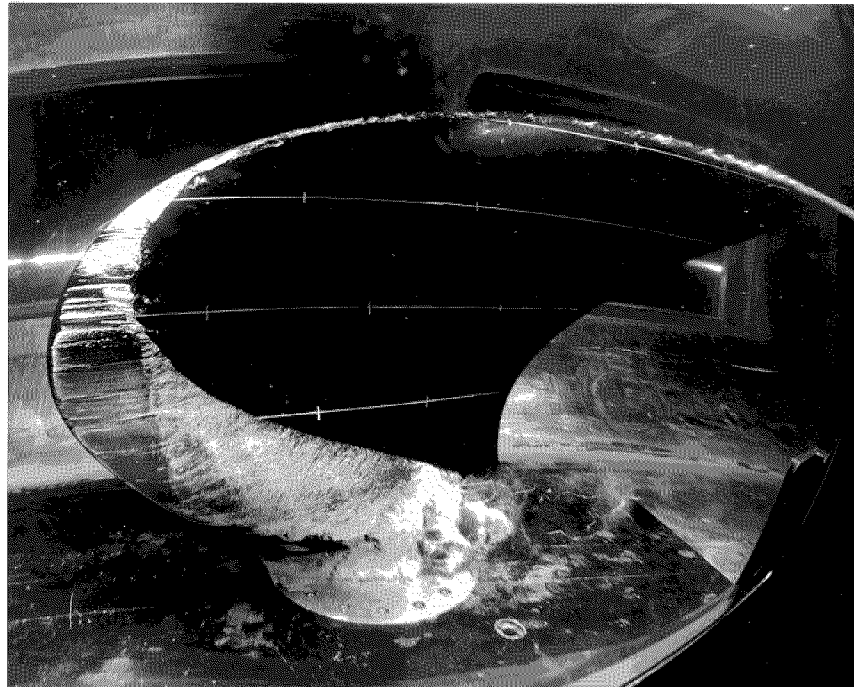


Figure 29: Photograph of the cavitating 4990 hydrofoil inside the DTMB 36inch cavitation tunnel; $\alpha = 0^\circ$, $\sigma = 0.62$. Courtesy of Dr. Rood of ONR and Dr. Jessup of DTMB. From (Kinnas et al 1998b).

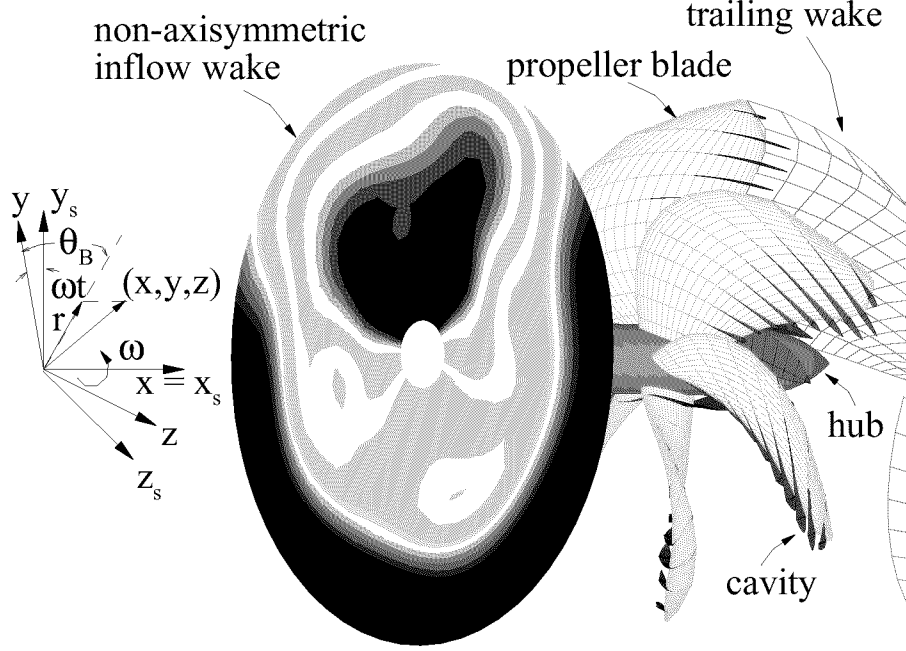


Figure 30: Propeller subjected to a general inflow wake. The propeller fixed (x, y, z) and ship fixed (x_s, y_s, z_s) coordinate systems are shown.

5 SUPER-CAVITATING PROPELLER

5.1 Formulation

This section summarizes the formulation of the cavitating flow around a propeller given by (Kinnas & Fine 1992) and (Fine 1992).

Consider a cavitating propeller subject to a general inflow wake, $\vec{q}_{wake}(x_s, y_s, z_s)$, as shown in Figure 30. The inflow wake is expressed in terms of the absolute (ship fixed) system of cylindrical coordinates (x_s, y_s, z_s) . The inflow velocity, \vec{q}_{in} , with respect to the propeller fixed coordinates (x, y, z) , can be expressed as the sum of the inflow wake velocity, \vec{q}_{wake} , and the propeller's angular velocity $\vec{\omega}$, at a given location \vec{x} :

$$\vec{q}_{in}(x, y, z, t) = \vec{q}_{wake}(x, r, \theta_B - \omega t) + \vec{\omega} \times \vec{x} \quad (94)$$

where $r = \sqrt{y^2 + z^2}$, $\theta_B = \arctan(z/y)$ and $\vec{x} = (x, y, z)$. The inflow, \vec{q}_{wake} , is assumed to be the *effective wake*, i.e. it includes the interaction between the vorticity in the inflow and the propeller (Choi 2000), (Choi & Kinnas 2001). The resulting flow is assumed to be incompressible and inviscid. The total velocity field, \vec{q} , can be expressed in terms of \vec{q}_{in} and the perturbation potential, ϕ , as follows:

$$\vec{q}(x, y, z, t) = \vec{q}_{in}(x, y, z, t) + \nabla \phi(x, y, z, t) \quad (95)$$

where ϕ satisfies the Laplace's equation in the fluid domain (i.e. $\nabla^2 \phi = 0$). Note that in analyzing the flow around the propeller, the propeller fixed coordinates system is used.

5.1.1 Green's formula

The perturbation potential, ϕ , at every point p on the combined wetted blade and cavity surface, $S_{WB}(t) \cup S_C(t)$, must satisfy Green's third identity:

$$2\pi\phi_p(t) = \int \int_{S_{WB}(t) \cup S_C(t)} \left[\phi_q(t) \frac{\partial G(p; q)}{\partial n_q(t)} - G(p; q) \frac{\partial \phi_q(t)}{\partial n_q(t)} \right] dS$$

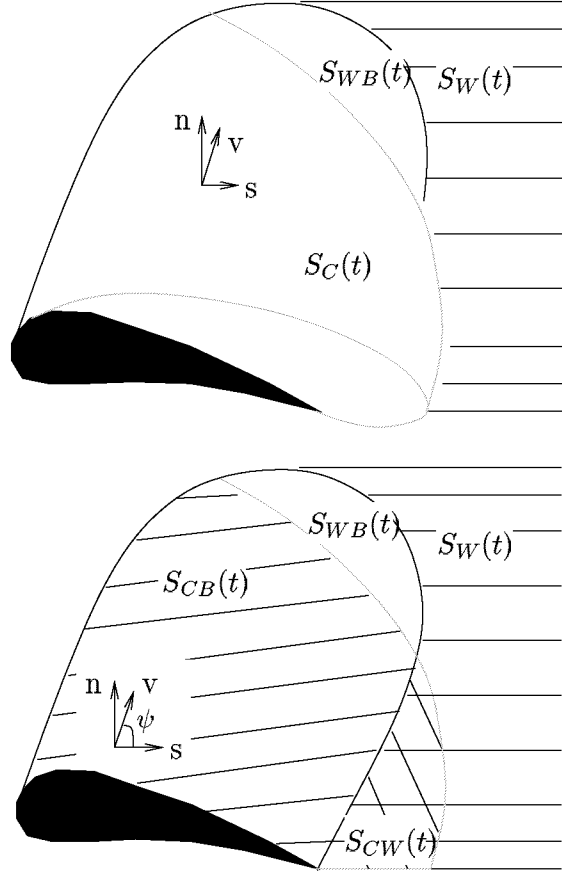


Figure 31: Top: Definition of the exact surface. Bottom: Definition of the approximated cavity surface.

$$+ \iint_{S_W(t)} \Delta\phi(r_q, \theta_q, t) \frac{\partial G(p; q)}{\partial n_q(t)} dS; \quad p \in (S_{WB}(t) \cup S_C(t)) \quad (96)$$

where the subscript q corresponds to the variable point in the integration. $G(p; q) = 1/R(p; q)$ is the Green's function with $R(p; q)$ being the distance between points p and q . \vec{n}_q is the unit vector normal to the integration surface. $\Delta\phi$ is the potential jump across the wake surface, $S_W(t)$. The definitions of S_{WB} , S_C and S_W are depicted in Fig. 31.

Eqn. 96 should be applied on the “exact” cavity surface S_C , as shown in the drawing at the top of Fig. 31. However, the cavity surface is not known and has to be determined as part of the solution. In this work, an approximated cavity surface, shown in the drawing at the bottom of Fig. 31, is used. The approximated cavity surface is comprised of the blade surface underneath the cavity on the blade, S_{CB} , and the portion of the wake surface which is overlapped by the cavity, S_{CW} . The justification for making this approximation, as well as a measure of its effect on the cavity solution can be found in (Kinnas & Fine 1993) and (Fine 1992).

Using the approximated cavity surface, Eqn. 96 may be decomposed into a summation of integrals over the blade surface, $S_B \equiv S_{CB} + S_{WB}$, and the portion of the wake surface which is overlapped by the cavity, S_{CW} .

Field Points on S_B .

For field points on S_B , Eqn. 96 becomes:

$$2\pi\phi_p(t) = \iint_{S_B} \left[\phi_q(t) \frac{\partial G(p; q)}{\partial n_q} - G(p; q) \frac{\partial \phi_q(t)}{\partial n_q} \right] dS \\ - \iint_{S_{CW}(t)} q_w(t) G(p; q) dS$$

$$+ \int \int_{S_{CW}(t) \cup S_W(t)} \Delta\phi(r_q, \theta_q, t) \frac{\partial G(p; q)}{\partial n_q} dS; \quad p \in S_B \quad (97)$$

where q_w is the cavity source distribution in the wake, defined as:

$$q_w(t) \equiv \frac{\partial \phi^+}{\partial n}(t) - \frac{\partial \phi^-}{\partial n}(t) \quad (98)$$

The superscripts "+" and "-" denote the upper and lower wake surface, respectively.

The geometry of the trailing wake is assumed to be invariant with time and taken to be the same as that corresponding to the circumferentially averaged flow (Kinnas & Hsin 1992). The dipole strength $\Delta\phi(r, \theta, t)$ in the wake is convected along the assumed wake model with angular speed ω :

$$\begin{aligned} \Delta\phi(r, \theta, t) &= \Delta\phi_T \left(r_T, t - \frac{\theta - \theta_T}{\omega} \right); \quad t \geq \frac{\theta - \theta_T}{\omega} \\ \Delta\phi(r, \theta, t) &= \Delta\phi^S(r_T); \quad t < \frac{\theta - \theta_T}{\omega} \end{aligned} \quad (99)$$

where r, θ are the cylindrical coordinates at any point in the trailing wake surface, S_W , and (r_T, θ_T) are the coordinates of the trailing edge at a point on the same streamline with (r, θ) . $\Delta\phi^S$ is the steady flow potential jump in the wake when the propeller is subject to the circumferentially averaged flow.

The value of the dipole strength, $\Delta\phi_T(r_T, t)$, at the trailing edge of the blade at radius r_T and time t , will be given from the Morino's Kutta condition (Morino & Kuo 1974):

$$\Delta\phi_T(r_T, t) = \phi_T^+(r_T, t) - \phi_T^-(r_T, t) = \Gamma(r_T, t) \quad (100)$$

where $\phi_T^+(r_T, t)$ and $\phi_T^-(r_T, t)$ are the values of the potential at the upper (suction side) and lower (pressure side) blade trailing edge, respectively, at time t . Γ is the circulation around the blade section.

Recently, an iterative pressure Kutta condition (Kinnas & Hsin 1992) is applied for the analysis of unsteady fully wetted and cavitating propellers. The iterative pressure Kutta condition modifies $\Delta\phi_T(r_T, t)$ from that of Morino to achieve equality of pressures at both sides of the trailing edge everywhere on the blade (Young et al 2001).

Field Points on S_{CW} .

For field points on S_{CW} , the left-hand side of Eqn. 96 reduces to $2\pi[\phi_p^+(t) + \phi_p^-(t)]$, which can be expressed as $4\pi\phi_p^\pm(t) \mp 2\pi\Delta\phi_p(t)$ depending on if the equation is applied on the upper "+" or the lower "-" surface of the supercavitating region. This will render the following expression for ϕ_p^\pm :

$$\begin{aligned} 4\pi\phi_p^\pm(t) &= \pm 2\pi\Delta\phi_p(t) \\ &+ \int \int_{S_B} \left[\phi_q(t) \frac{\partial G(p; q)}{\partial n_q} - G(p; q) \frac{\partial \phi_q(t)}{\partial n_q} \right] dS \\ &- \int \int_{S_{CW}(t)} q_w(t) G(p; q) dS \\ &+ \int \int_{S_{CW}(t) \cup S_W(t)} \Delta\phi(r_q, \theta_q, t) \frac{\partial G(p; q)}{\partial n_q} dS; \quad p \in S_{CW} \end{aligned} \quad (101)$$

5.1.2 Kinematic Boundary Condition on Wetted Part of the Blade

The kinematic boundary condition on the wetted portion of the blade defines the source strengths in terms of the known inflow velocity, \vec{q}_{in} :

$$\frac{\partial \phi_q}{\partial n_q} = -\vec{q}_{in}(x_q, y_q, z_q, t) \cdot \vec{n}_q \quad (102)$$

5.1.3 Dynamic Boundary Condition on Cavitating Surfaces

The dynamic boundary condition on the cavitating blade and wake surfaces requires the pressure everywhere on the cavity to be constant and equal to the vapor pressure, P_v . By applying Bernoulli's equation, the total velocity on the cavity, \vec{q}_c , can be expressed as follows:

$$\vec{q}_c^2 = n^2 D^2 \sigma_n + |\vec{q}_{wake}|^2 + \omega^2 r^2 - 2gy_s - 2\frac{\partial\phi}{\partial t} \quad (103)$$

where $\sigma_n \equiv (P_o - P_v)/(\frac{\rho}{2}n^2 D^2)$ is the cavitation number; ρ is the fluid density and r is the distance from the axis of rotation. P_o is the pressure far upstream on the shaft axis; g is the acceleration of gravity and y_s is the ship fixed coordinate, shown in Fig. 30. $n = \omega/2\pi$ and D are the propeller rotational frequency and diameter, respectively.

On the cavitating blade surface, the magnitude of the cavity velocity may also be written in terms of its projections along \vec{s} (the chordwise) and \vec{v} (the spanwise) grid directions on the blade surface:

$$|\vec{q}_c| \sin \psi = \sqrt{V_s^2 + V_v^2 - 2V_s V_v \cos \psi} \quad (104)$$

with:

$$V_s \equiv \frac{\partial\phi}{\partial s} + \vec{q}_{in} \cdot \vec{s} \quad \text{and} \quad V_v \equiv \frac{\partial\phi}{\partial v} + \vec{q}_{in} \cdot \vec{v} \quad (105)$$

where ψ is the angle between s and v directions, as shown in Fig. 31.

Combining Eqns. 103 and 104 renders the following expression for $\frac{\partial\phi}{\partial s}$:

$$\frac{\partial\phi}{\partial s} = -\vec{q}_{in} \cdot \vec{s} + V_v \cos \psi + \sin \psi \sqrt{|\vec{q}_c|^2 - V_v^2} \quad (106)$$

which can then be integrated to form a Dirichlet type boundary condition for ϕ . The unknown terms $\frac{\partial\phi}{\partial t}$ and $\frac{\partial\phi}{\partial v}$ on the right-hand side of Eqn. 106 are determined in an iterative manner.

On the cavitating wake surface, the coordinate \vec{s} is assumed to follow the streamline¹⁵. Thus, the total cross flow velocity is assumed to be small, which renders the following expression for $\frac{\partial\phi}{\partial s}$:

$$\frac{\partial\phi}{\partial s} = -\vec{q}_{in} \cdot \vec{s} + |\vec{q}_c| \quad (107)$$

5.1.4 Kinematic Boundary Condition on Cavitating Surfaces

The kinematic boundary condition on the cavity requires the total velocity normal to the cavity to be zero. As shown in (Kinnas & Fine 1992), the kinematic boundary condition renders the following equation for the cavity thickness (h) on the blade:

$$\frac{\partial h}{\partial s} [V_s - \cos \psi V_v] + \frac{\partial h}{\partial v} [V_v - \cos \psi V_s] = \sin^2 \psi \left(V_n - \frac{\partial h}{\partial t} \right) \quad (108)$$

where $V_n \equiv \frac{\partial\phi}{\partial n} + \vec{q}_{in} \cdot \vec{n}$ is the total normal velocity.

Assuming again that the spanwise crossflow velocity on the wake surface is small, the kinematic boundary condition reduces to the following equation for the cavity thickness (h_w) on the wake:

$$q_w(t) - \frac{\partial h_w}{\partial t} = |\vec{q}_c| \frac{\partial h_w}{\partial s} \quad (109)$$

where q_w is the cavity source distribution, defined by Eqn. 98.

The definitions of h and h_w are depicted in Fig. 32. The quantity h_w at the blade trailing edge is determined by interpolating the upper cavity surface over the blade and computing its normal offset from the wake sheet.

¹⁵It has been found by (Fine 1992) (Fine & Kinnas 1993b) that the effect of the crossflow term in the cavitating wake region has very little effect on the solution.

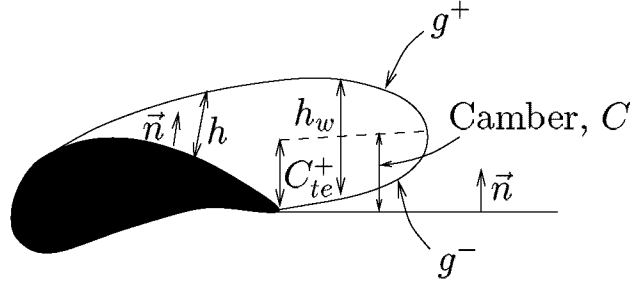


Figure 32: Definition of the cavity height on the blade and on the supercavitating wake.

5.1.5 Cavity Closure Condition

The extent of the unsteady cavity is unknown and has to be determined as part of the solution. The cavity length at each radius r is given by the function $l(r, t)$. For a given cavitation number, σ_n , the cavity planform $l(r, t)$ must satisfy the following requirement:

$$\delta(l(r, t), r; \sigma_n) \equiv h(l(r, t), r, t) = 0 \quad (110)$$

where δ is the cavity height at the trailing edge of the cavity. Eqn. 110 requires that the cavity closes at its trailing edge. This requirement is the basis of an iterative solution method that is used to find the cavity planform.

5.1.6 Solution Method

The unsteady cavity problem is solved by inverting Eqns. 97 and 101 subjected to conditions 99, 100, 102, 106, 107, and 110. The numerical implementation is described in detail in (Kinnas & Fine 1992), (Fine 1992), and (Kinnas & Fine 1993). In brief, for a given cavity planform, Green's formula is solved with respect to the unknown ϕ on the wetted blade surface and the unknown $\frac{\partial \phi}{\partial n}$ on the cavity surface. The cavity heights are then determined by integrating Eqns. 108 and 109. The correct cavity planform is obtained in an iterative manner by satisfying the cavity closure condition, Eqn. 110. The split-panel technique (Fine & Kinnas 1993a) (Kinnas & Fine 1993) is used to treat blade and wake panels that are intersected by the cavity trailing edge. Systematic convergence studies for various propeller geometries and flow conditions, as well as several comparisons with existing experiments of propellers in steady, unsteady, and cavitating flow are presented in (Young & Kinnas 2001).

5.2 Validation with experiments

In order to thoroughly validate PROPCAV, results from four different sets of experiments are presented.

To validate the supercavitation scheme in PROPCAV, predicted force coefficients are compared with experimental measurements (Matsuda et al 1994) for a supercavitating propeller. The test geometry is M.P.No.345(SRI), which is designed using SSPA charts under the following conditions: $J_S = 1.10$, $\sigma_v = 0.40$, and $K_T = 0.160$. It should be noted that the current version of PROPCAV modifies the suction side of the blade section aft of the midchord to render zero thickness at the trailing edge. This modification should not affect the results as long as the blade sections aft of the midchord are within the cavitation bubble.

The comparisons of the predicted versus measured thrust (K_T), torque (K_Q), and efficiency (η_p) are shown in Figure 33. The propeller geometry with the predicted cavities at $J_S = 1.3$ are shown in Figure 34. Also shown in Figure 34 are the predicted cavitating pressures along each radial strip at $J_S = 1.3$. It is worth noting that at this particular combination, there is substantial midchord detachment. Figure 34 indicates that the detachment search criterion in PROPCAV, which will be explained later, is satisfied since the cavity thickness is non-negative and the pressures everywhere on the wetted blade surfaces are above the vapor pressure. The comparisons shown on Figure 33 indicate that the predictions by PROPCAV agree very well with experimental data for values of $J_S \leq 1.2$. For $J_S > 1.2$, the comparisons are not as good because the cavities begin to detach aft of the midchord, where the suction side geometry was modified.

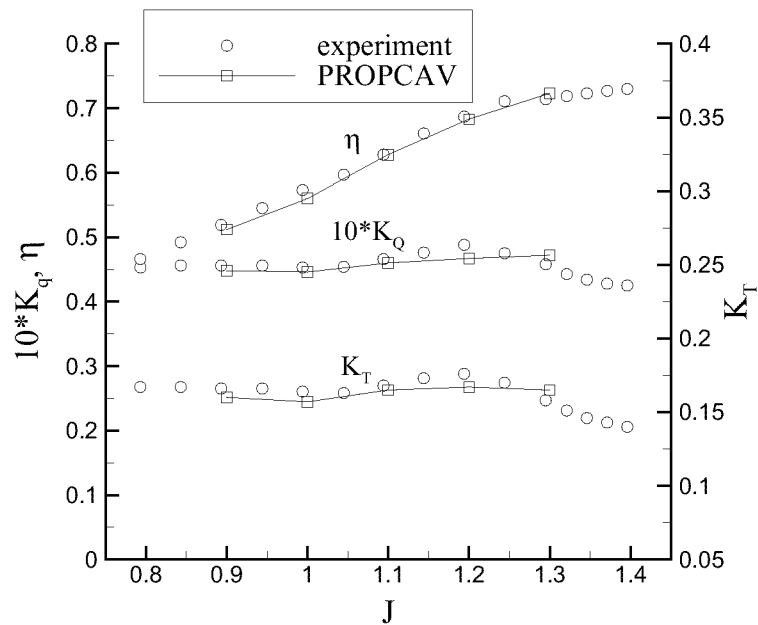


Figure 33: Comparison of the predicted and versus measured K_T , K_Q , and η for different advance coefficients. From (Young & Kinnas 2001).

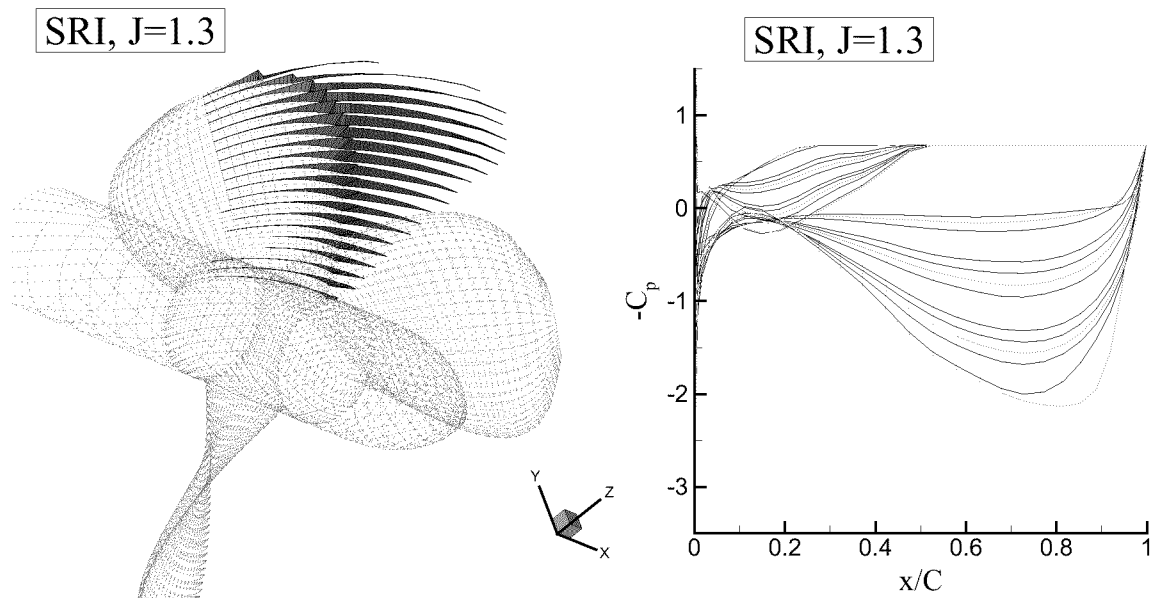


Figure 34: Geometry, cavitation pattern, and cavitating pressures for propeller SRI at $J_S = 1.3$. $\sigma_v = 0.4$. $\sigma_n = \sigma_v \times J_S^2$. From (Young & Kinnas 2001).

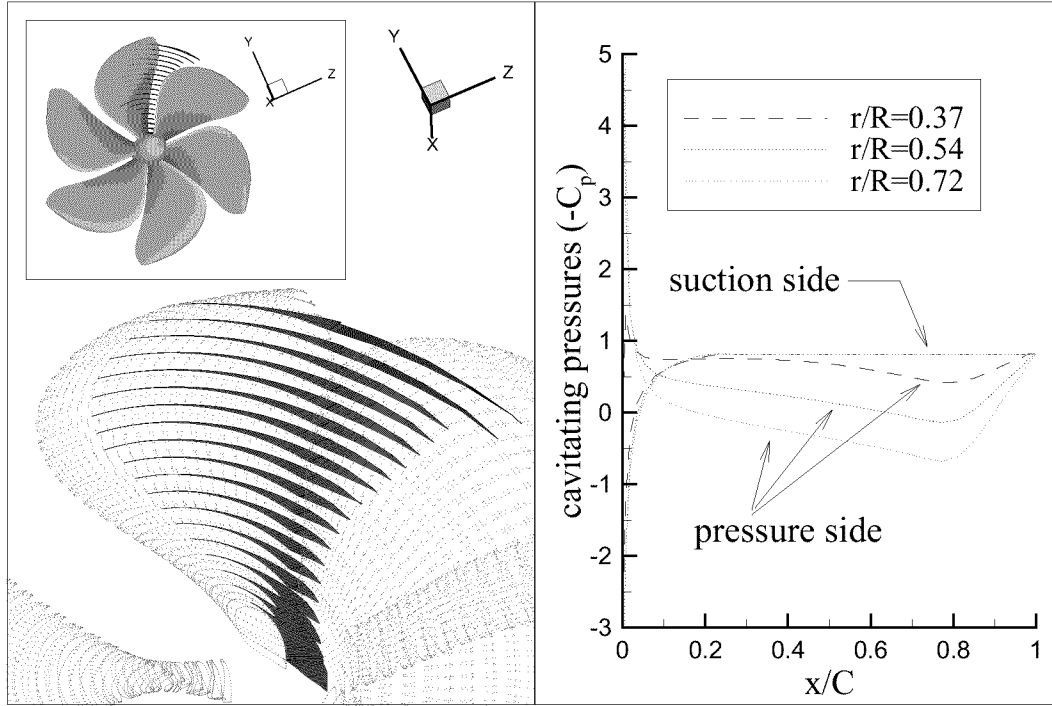


Figure 35: Cavity shape and pressures for propeller MW1. Mid-chord cavitation. The propeller is based on a design by Michigan Wheel Corporation, USA. $J_S = 1.224$. $\sigma_n = 0.8116$. $F_r = 26.6$. 60x20 panels. Uniform inflow. From (Young & Kinnas 2001).

5.3 Mid-chord detachment

The latest version of PROPCAV allows the cavity to detach from both the face (pressure side) and the back (suction side) of the blade. The initial detachment lines are obtained based on the fully wetted pressures. The detachment locations at each strip are then adjusted in the next revolution¹⁶ according to the following criterion:

1. If the cavity at the strip has negative thickness, then the detachment location is moved towards the trailing edge of the blade.
2. If the pressure at a point upstream of the cavity is below the vapor pressure, then the detachment location is moved towards the leading edge of the blade.

It can be shown that the above criterion is equivalent to the Villat-Brillouin smooth detachment condition. Details of the formulation and convergence study for mid-chord detachment can be found in (Mueller 1998) and (Mueller & Kinnas 1999). An example of mid-chord cavitation for propeller MW1¹⁷ subjected to uniform inflow ($J_S = 1.224$, $\sigma = 0.8116$, $F_r = 26.6$) is shown in Fig. 35. Also shown in Fig. 35 are the corresponding cavitating pressures at three different strips along the span of the blade. It is worth noting that the predicted pressures on the suction side in front of the cavity detachment are higher than the vapor pressure. This indicates that the employed smooth detachment criterion works properly. However, the face side cavitating pressures near the leading edge are below the vapor pressure. This is because PROPCAV was only allowed to search for back cavitation. Had the option to search for face and back cavitation simultaneously (as explained in the next section) been on, PROPCAV would have also detected the expected face cavitation as shown in Figure 38.

5.4 Face and back cavitation

The latest version of PROPCAV allows the cavity to grow on both sides of the blade simultaneously. In this case, the dynamic boundary condition is applied on both cavity surfaces, and the kinematic boundary condition

¹⁶The solution is carried out over several complete revolutions of one blade, the “key” blade, with the effects of the other blades being accounted for in an iterative manner.

¹⁷The propeller geometry is based on a design by Michigan Wheel Corporation, USA (Young & Kinnas 2001).

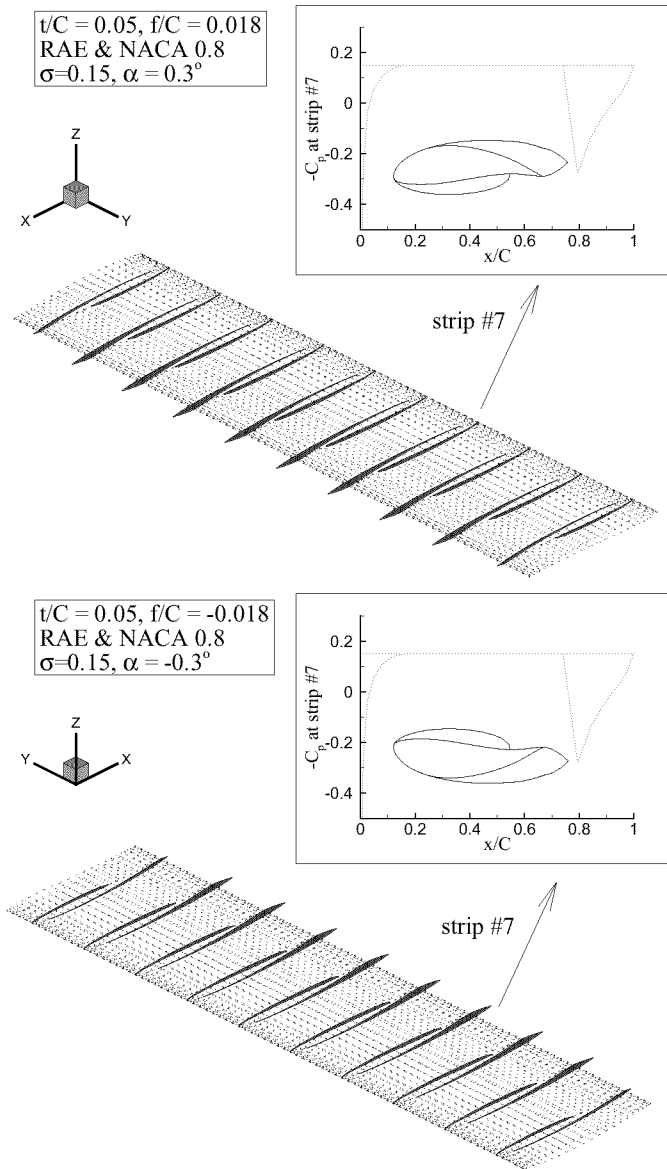


Figure 36: Validation of simultaneous face and back cavitation on an asymmetric rectangular hydrofoil. 50X10 panels. $\alpha = \pm 0.3^\circ$. $f/C = \pm 0.018$ (NACA0.8). $t/C = 0.05$ (RAE). $\sigma_v = 0.15$. From (Young & Kinnas 2001).

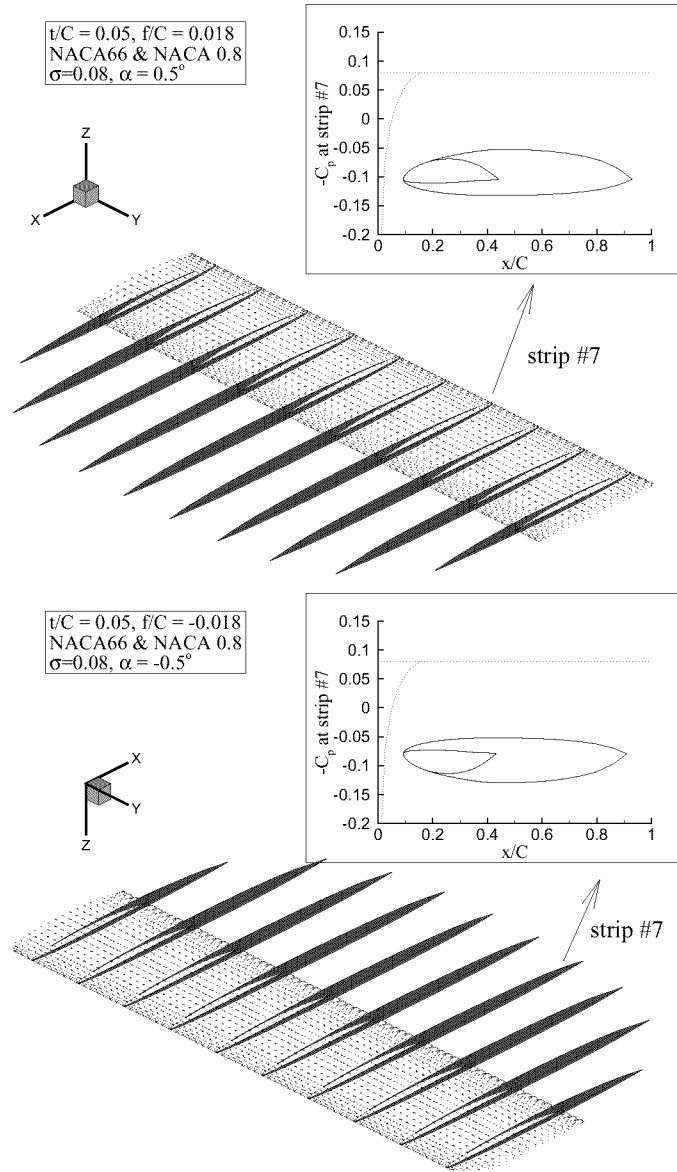


Figure 37: Validation of simultaneous face and back cavitation on an asymmetric rectangular hydrofoil. 50X10 panels. $\alpha = \pm 0.5^\circ$. $f/C = \pm 0.018$ (NACA0.8). $t/C = 0.05$ (NACA66). $\sigma_v = 0.08$. From (Young & Kinnas 2001).

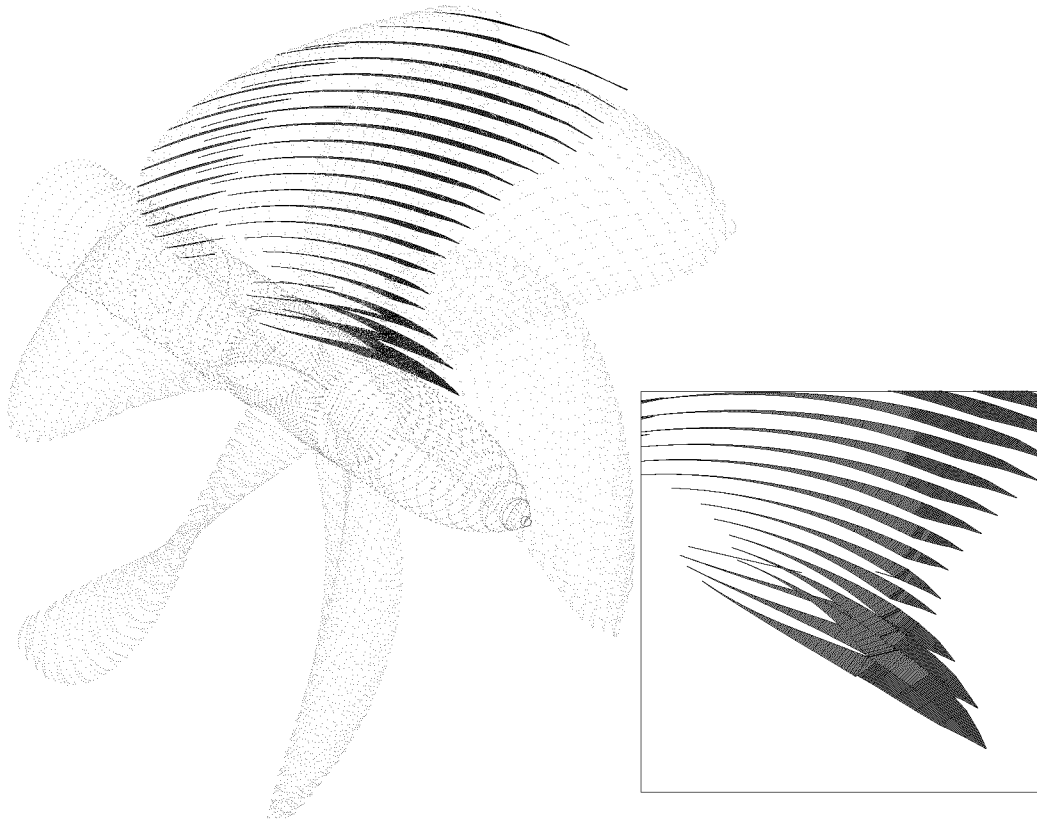


Figure 38: Predicted 3-D cavity shape for propeller MW1. The propeller is based on a design by Michigan Wheel Corporation, USA. 60x20 panels. $J_S = 1.224$. $\sigma_n = 0.8116$. $F_r = 25.6$. Uniform inflow. From (Young & Kinnas 2001).

is applied on the wetted blade surfaces. PROPCAV also has the ability to search for cavity detachments on both sides of the blade simultaneously.

Validation test for an asymmetric 3-D hydrofoil¹⁸ with $\pm 1.8\%$ camber (f/C) and $\sigma_v = 0.15$ (based on the speed of the uniform inflow) at an angle of attack of $\pm 0.3^\circ$ is shown in Figure 36. As expected, the predicted cavity shapes are identical mirror images of each other. The same validation test was performed for another asymmetric 3-D hydrofoil at an angle of attack of $\pm 0.5^\circ$ with $\pm 1.8\%$ camber and $\sigma_v = 0.08$. The results are shown in Figure 37. Note that for both cases, the smooth detachment criterion are satisfied on both sides of the 3-D hydrofoil.

An example of simultaneous face and back cavitation for propeller MW1 is shown in Figure 38. The propeller geometry is based on a design by Michigan Wheel Corporation, USA (Young & Kinnas 2001). The flow conditions were as follows: $J_S = 1.224$, $\sigma_n = 0.8116$, uniform inflow. Notice that for this propeller, there is midchord supercavitation on the suction side of the blade, and leading partial cavitation as well as midchord supercavitation on the pressure side of the blade. To validate the solution, the convergence of the predicted cavities (on the back side of the blade) and forces with respect to the number of panels are shown in Figure 39.

¹⁸For validation studies, PROPCAV has an option where the numerical method is applied on a 3-D hydrofoil.

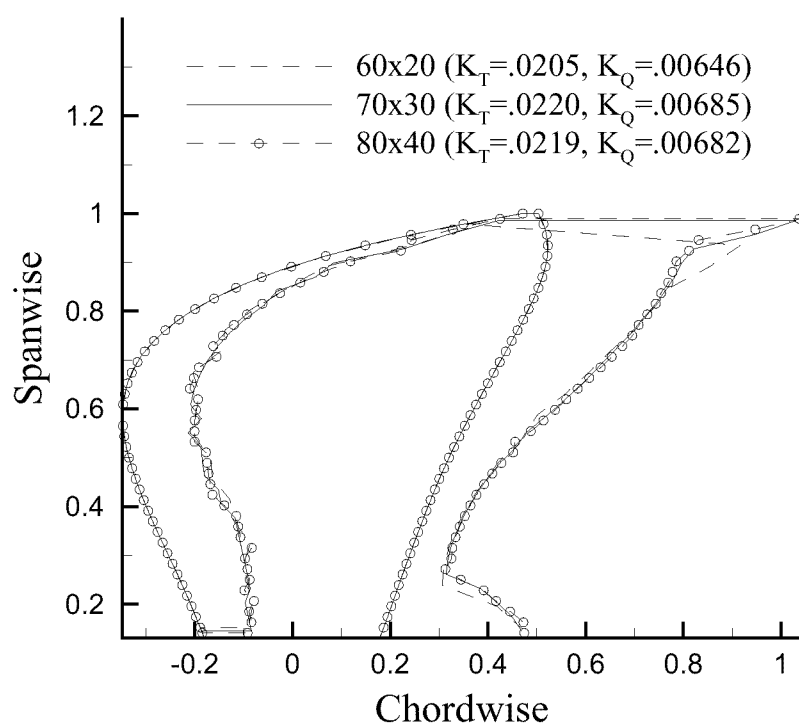
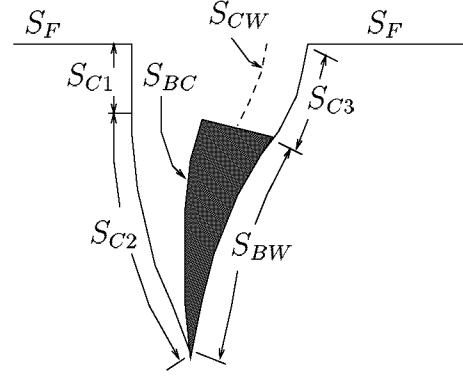


Figure 39: The convergence of predicted cavities (expanded view) and forces with respect to number of panels for propeller MW1. The propeller is based on a design by Michigan Wheel Corporation, USA. $J_S = 1.224$. $\sigma_n = 0.8116$. $F_r = 25.6$. Uniform inflow. From (Young & Kinnas 2001).



$$S \equiv S_F \cup S_{C1} \cup S_{C2} \cup S_{C3} \cup S_{BW}$$

Figure 40: Definition of exact and approximated flow boundary

6 SURFACE-PIERCING PROPELLER

6.1 Formulation

Consider a surface-piercing propeller subjected to a general non-axisymmetric inflow. For incompressible and inviscid flow, the perturbation potential, ϕ , at any time t satisfies Laplace's equation in the fluid domain:

$$\nabla^2 \phi(x, y, z, t) = 0 \quad (111)$$

where (x, y, z) are the propeller fixed coordinates.

The perturbation potential, ϕ_p , at every point p on the combined wetted blade surface (S_{BW}), ventilated cavity surface ($S_{C1} \cup S_{C2} \cup S_{C3}$), and free surface (S_F), must satisfy Green's third identity:

$$2\pi\phi_p(t) = \iint_{S(t)} \left[\phi_q(t) \frac{\partial G(p; q)}{\partial n_q(t)} - G(p; q) \frac{\partial \phi_q(t)}{\partial n_q(t)} \right] dS \quad (112)$$

where $S \equiv (S_{BW} \cup S_{C1} \cup S_{C2} \cup S_{C3} \cup S_F)$ is the combined surfaced as defined in the blade section example shown on Figure 40. The subscript q corresponds to the variable point in the integration. $G(p; q) = 1/R(p; q)$ is Green's function with $R(p; q)$ being the distance between points p and q . \vec{n}_q is the unit vector normal to the integration surface.

Equation 112 should be applied on the “exact” cavity surface¹⁹ ($S_{C1} \cup S_{C2} \cup S_{C3}$), as shown in Figure 40. However, the cavity surface is not known and has to be determined as part of the solution. In this work, an approximated cavity surface (on which the panels of the boundary element method are placed) is used. The approximated cavity surface is comprised of the blade surface underneath the cavity on the blade, $S_{C2} \rightarrow S_{BC}$, and the portion of the wake surface which is overlapped by the cavity, $(S_{C1} \cup S_{C3}) \rightarrow S_{CW}$. The definition of S_{BC} and S_{CW} are also shown in Figure 40. The justification for making this approximation, as well as a measure of its effect on the cavity solution, can be found in (Kinnas & Fine 1993) and (Fine 1992).

6.1.1 Linearized free surface boundary condition on the free surface, S_F

The linearized free surface boundary condition requires that:

$$\frac{\partial^2 \phi}{\partial t^2} + g \frac{\partial \phi}{\partial \eta} = 0 \quad (113)$$

where η is the free surface elevation. Assuming infinite Froude number condition applies, Equation 113 reduces to:

$$\phi = 0 \quad \text{on the free surface} \quad (114)$$

¹⁹The ventilated surface will be referred to as the cavity surface in this work.

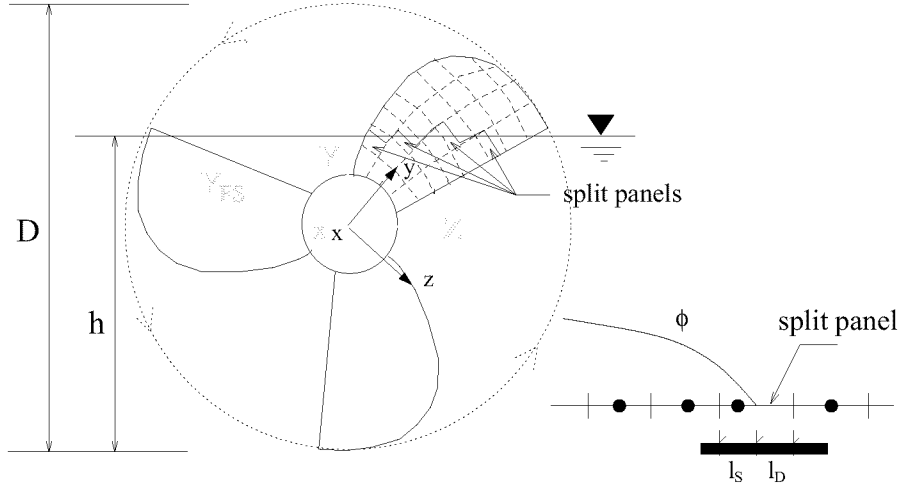


Figure 41: Definition of global (X,Y,Z) and local (x,y,z) coordinate systems and parameters for the split-panel technique.

Equation 114 implies that the “negative” image method can be used to account for the effect of the free surface. The infinite Froude number assumption is valid because surface-piercing propellers usually operate at very high speeds. (Shiba 1953) and (Yim 1974) have also concluded that gravity effects are negligible for Froude numbers greater than 3.

6.2 Solution algorithm

The unsteady ventilated cavity problem is solved by inverting equations 97 and 101 (where S_W should be eliminated from the limits of the integrals) subjected to the boundary conditions 99, 100, 108, 109, 106 (where σ_n in the expression for q_c , equation 103, must be evaluated by replacing P_v with the atmospheric pressure, P_{atm} , as this is the pressure inside the ventilated surface), and 114 (enforced via the negative images of the panels). On the wetted blade surface, ϕ is unknown and $\frac{\partial\phi}{\partial n}$ is known. On the ventilated cavity surface, ϕ is known and $\frac{\partial\phi}{\partial n}$ is unknown. To simplify the solution algorithm, ϕ and $\frac{\partial\phi}{\partial n}$ on the “dry” part of blades are set equal to zero. Thus, the number of unknowns is reduced to the number of fully submerged panels on the blade and on the wake. After solving Equations 97 and 101, the cavity heights are then determined by applying the kinematic boundary condition (Equation 108) on the ventilated cavity surface.

6.2.1 Split-panel technique

One of the difficulties in the numerical modeling of surface-piercing propellers involves the discretization of the blade and wake surfaces. The nature of the problem is highly unsteady due to the blades’ entry to and exit from the free surface. The split-panel technique, which was introduced by (Kinnas & Fine 1993) for approximating the trailing edge of cavity planform. The partially submerged panels are *split* into a dry part and a submerged part, as shown in Figure 41. The lengths of the split-panels at their midspans are l_D and l_S , respectively. The source and dipole strengths on the split-panels (ϕ_{sp} and $\frac{\partial\phi}{\partial n}_{sp}$) are defined as weighted averages of the values on the dry part and the submerged part of the panel:

$$\begin{aligned}\phi_{sp} &= \frac{\phi_S l_S + \phi_D l_D}{l_S + l_D} \\ \frac{\partial\phi}{\partial n}_{sp} &= \frac{\frac{\partial\phi}{\partial n}_S l_S + \frac{\partial\phi}{\partial n}_D l_D}{l_S + l_D}\end{aligned}\quad (115)$$

The quantities ϕ_D and $\frac{\partial\phi}{\partial n}_D$ are set equal zero because they represent the dry part of the panel. If the split-panel is located on the wetted side of the blade, then $\frac{\partial\phi}{\partial n}_S$ is known via the kinematic boundary condition (Equation 89) and ϕ_S is extrapolated from adjacent panels; if the split-panel is located on the ventilated side of the blade, then ϕ_S is known via the dynamic boundary condition (Equation 103) and $\frac{\partial\phi}{\partial n}_S$ is extrapolated from adjacent panels.

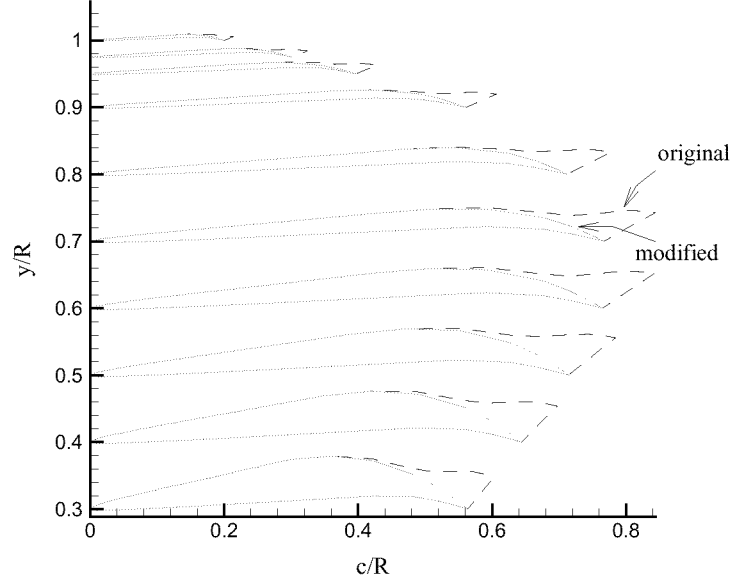


Figure 42: Original and modified (on the suction side aft the midchord) blade section geometry of propeller model 841-B.

The split-panel technique has the advantage that it allows the free surface to be relatively smooth without the added burden of recomputing influence coefficients at every timestep.

6.3 Results

In order to validate the new extension of PROPCAV, numerical results for the surface-piercing propeller model 841-B, already shown in Figure 3, are compared with experimental data. The experiments were conducted at the free-surface cavitation tunnel at KaMeWa of Sweden (Olofsson 1996). The flow conditions were as follows:

$$\begin{aligned}
 \text{advance coefficient:} & \quad J_S = 0.8 \\
 \text{submergence ratio:} & \quad h/D = 0.33 \\
 \text{shaft yaw angle:} & \quad \psi = 0^\circ \\
 \text{shaft inclination angle:} & \quad \gamma = 0^\circ
 \end{aligned}$$

In the numerical calculation, the blade section was modified from the original aft of the midchord, as shown in Figure 42, in order to render zero trailing edge thickness. Furthermore, the code is still in the developmental stage. Thus, the current results do not include the effect of the partially submerged panels.

Preliminary force predictions for propeller model 841-B are shown in Figure 43 along with experimental data from (Olofsson 1996). The solid lines in Figure 43 represent the force coefficients predicted by PROPCAV at different blade angles. The symbols in Figure 43 represent the measured force coefficients. As shown in Figure 43, the maximum force coefficients predicted by PROPCAV seemed to be in reasonable agreement with experimental measurements. However, there are discrepancies at the blade entry and exit. The authors believe that the discrepancies at the blade entry are due to the effects of free surface up-ward jets and blade vibrations, both of which are not captured with the current numerical model. The discrepancies at the blade exit are probably due to the modified blade sections aft of the midchord and the change in free surface elevation. The sensitivity of the results on the discretization parameters can be found in (Young & Kinnas 2000).

The fully submerged panels for the key blade are shown in Figure 44. The resulting pressure contours on the wetted side of the blade are depicted in Figure 45. The predicted ventilated surface sections at different timesteps are shown in Figure 46.

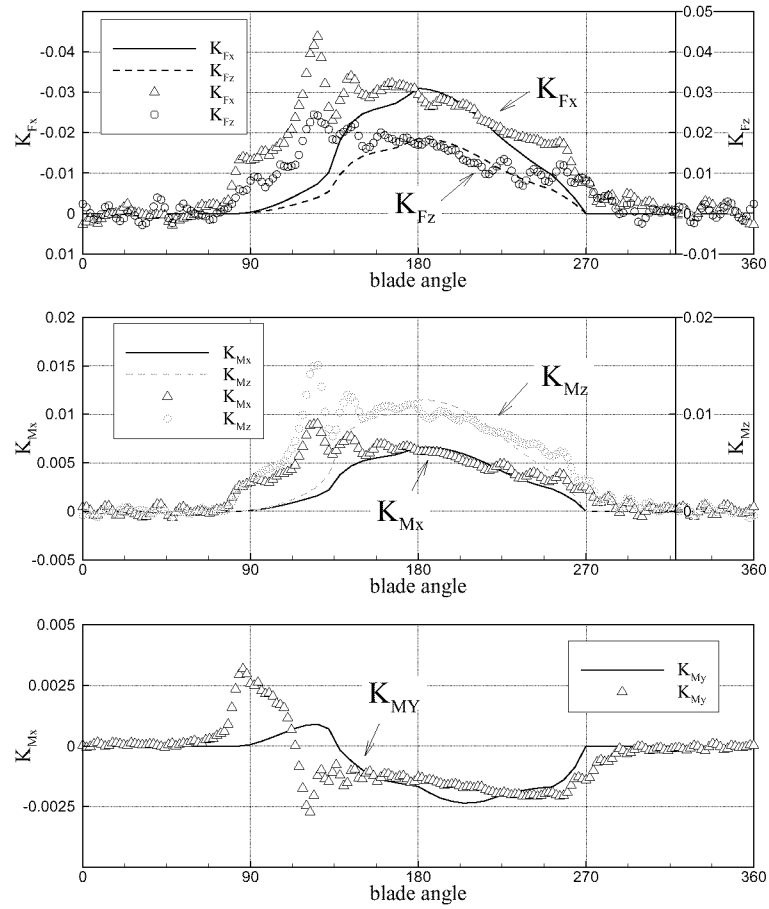


Figure 43: Preliminary comparison of the blade forces predicted by PROPCAV and by measurements from experiments. Propeller model 841-B. 4 Blades. $h/D = 0.33$. $J_S = 0.8$. 60x20 panels. $\Delta\theta = 6^\circ$.

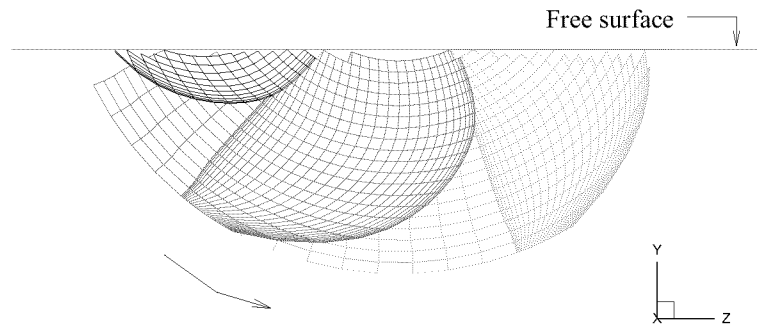


Figure 44: Fully submerged panels on the key blade at different time steps. Propeller model 841-B. 4 Blades. $h/D = 0.33$. $J_S = 0.8$. 60x20 panels. $\Delta\theta = 6^\circ$.

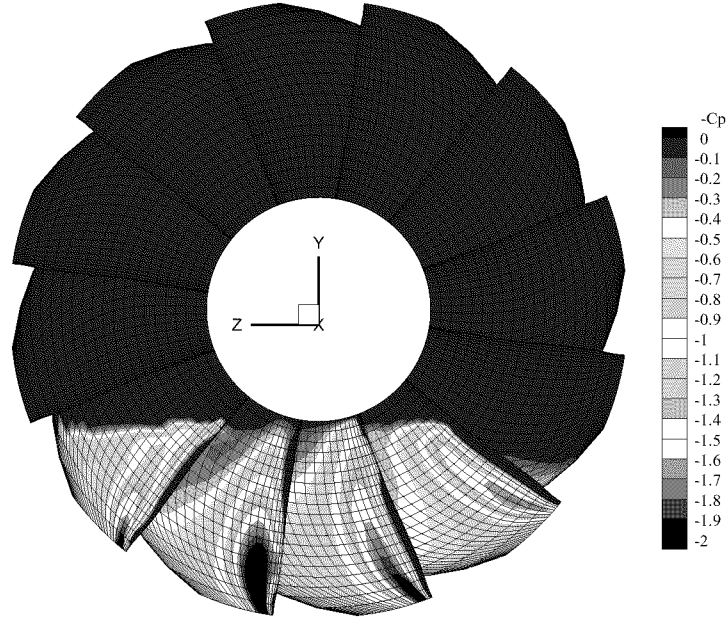


Figure 45: Preliminary pressure contours predicted by PROPCAV. Propeller model 841-B. 4 Blades. $h/D = 0.33$. $J_S = 0.8$. 60x20 panels. $\Delta\theta = 6^\circ$.

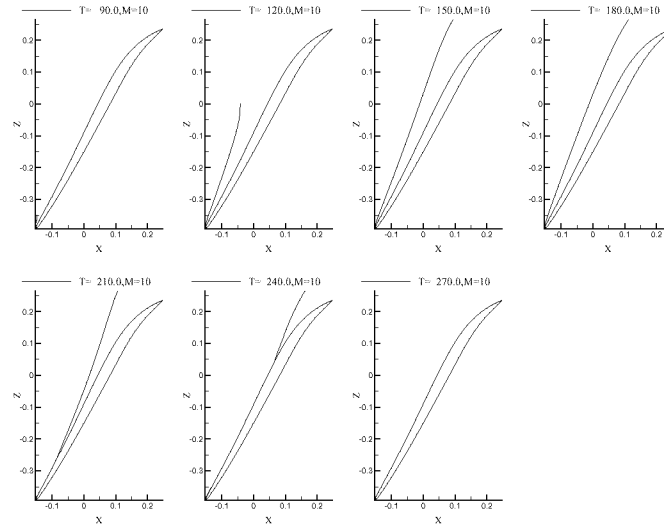


Figure 46: Preliminary ventilated surface sections at $r/R = 0.52$. Propeller model 841-B. 4 Blades. $h/D = 0.33$. $J_S = 0.8$. 60x20 panels. $\Delta\theta = 6^\circ$.

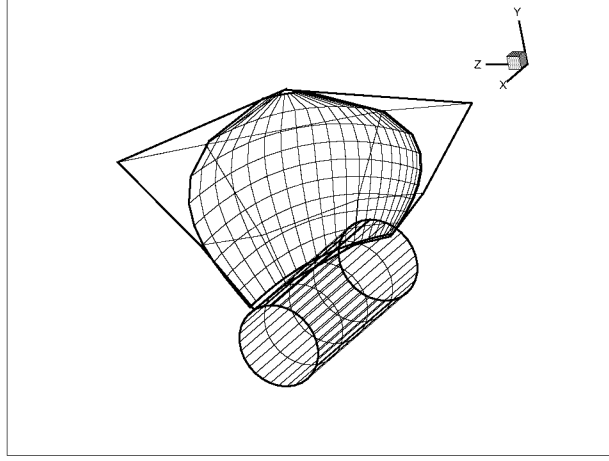


Figure 47: B-spline polygon and the paneled blade geometry in CAVOPT-3D/MPUF-3A.

7 DESIGN OF SUPER-CAVITATING PROPELLER

An optimization method (CAVOPT-3D), similar to that for supercavitating hydrofoil sections, has been developed (Mishima 1996, Mishima & Kinnas 1997). The coefficients of the objective function are determined in terms of second order Taylor expansions from the results of MPUF-3A, a vortex and source lattice method for cavitating propellers in unsteady flow (Kinnas et al 1998a). This method determines *both* the optimum cavitating propeller loading *and* the corresponding blade geometry at the same time. The blade mean camber surface is modeled with a 4x4 cubic B-spline vertex polygon net (Mishima 1996) (Griffin 1998), as shown in Figure 47. This allows the blade surface to be modeled with relatively few number of parameters when compared with the traditional method²⁰ of describing the blade geometry. The location of each of the B-Spline vertices, and thus the radial chord distribution, as well as the three-dimensional blade camber distribution, are determined during the design process. The skew distribution can be either fixed or specified (as parabolic or linear) up to a constant which can be also determined by the optimization. The maximum thickness to diameter ratio along the radial direction must be specified (using structural criteria) together with the blade thickness section shapes.

The objective function to be minimized is:

$$f(\mathbf{x}) = K_Q(\mathbf{x})$$

where $K_Q(\mathbf{x})$ is the torque coefficient obtained from *MPUF-3A* (Kinnas et al 1998a) and \mathbf{x} is the design variable vector defining the the blade B-spline polygon (usually 13).

$$\mathbf{x} = [x_1, x_2, x_3, \dots, x_{13}]^T$$

The equality constraint function is defined as

$$h_1(\mathbf{x}) = \frac{K_T(\mathbf{x}) - K_{To}}{K_{To}} = 0$$

where K_{To} is the required thrust coefficient and $K_T(\mathbf{x})$ is the computed thrust coefficient from *MPUF-3A*. The functions of the equality and inequality constraints are denoted as $h_i(\mathbf{x})$ and $g_i(\mathbf{x})$, respectively. *CAVOPT-3D* currently has the option of employing five inequality constraints, defined as

$$\begin{aligned} \text{Cavity area} &\leq CMAX \\ \text{Face cavity area} &\leq FMAX \end{aligned}$$

²⁰Span-wise values of pitch, rake, skew, chord, maximum thickness, maximum camber and chord-wise distributions of camber and thickness.

$$\begin{aligned}
Max.skew &\leq SKMAX \\
Cavity\ volume\ velocity &\leq VVMAX \\
\sigma_n - (-C_{p,min}) &> PTOL
\end{aligned} \tag{116}$$

where the values on the left hand side are the values computed from *MPUF-3A* and the values on the right hand side are the user-specified limits to the left hand side values. The cavity area constraints CAMAX and FAMAX represent the maximum allowable back and face cavity area (as a fraction of the blade area), respectively. VVMAX corresponds to the maximum allowable blade rate cavity volume velocity harmonic, non-dimensionalized by nR^3 . SKMAX corresponds to the maximum allowable skew at the tip of the blade. An option for quadratic or linear skew distribution is also available. $-C_{p,min}$ is the value of $-C_p$ at a location on the fully wetted part of the blade where the pressure is minimum (over all blade angles), and *PTOL* is a specified tolerance.

The required input design variables required by *CAVOPT-3D* to set-up the design model are given as:

- advance coefficient (J_S)
- cavitation number (σ_n)
- Froude number (F_r)
- number of blades (Z)
- hub radius (r_H)
- required thrust coefficient (K_{To})
- inflow wake distribution

7.1 Application

The 3-D method has been applied extensively for the design of conventional propellers (Griffin & Kinnas 1998), (Kinnas et al 1999b), and more recently for the design of a supercavitating propeller (Kinnas et al 1999a). The SRI propeller Model No. 345 (Kudo & Ukon 1994), is used as the base for the supercavitating propeller design. It is identified here as the SRI/SSPA propeller, since the SSPA charts (Rutgersson 1979) were used to design it.

The original thickness distribution, as shown in Figure 48 has been used as input in *CAVOPT-3D*. We have forced leading-edge cavity detachment in *MPUF-3A*. The same design conditions as those of the SRI propeller are used for *CAVOPT-3D*.

These are:

$$\begin{aligned}
J_S &= 1.1, \sigma_n = 0.484, F_r = 5.0 \\
Z &= 3, r_H/R = 0.19, K_{To} = 0.175
\end{aligned}$$

Uniform inflow is used. For these conditions MPUF-3A predicts $K_T = 0.175$ and $\eta = 69.4\%$. The corresponding predicted cavity planform is shown in Figure 49.

The designed geometry by CAVOPT-3D is shown in Figures 50, 51, while a summary sheet from the design run is shown in Figure 52 (in which the predicted cavity planform is shown at the lower right bottom).

The following things should be noted:

- The new design has a substantially larger efficiency, 74.7%, i.e. increase in efficiency of over 7%.
- The new design has a wider blade area and a lower pitch (for the same thrust)
- The predicted cavities for the new design are thinner at the leading edge as well as at the trailing edge, thus resulting into a smaller cavity drag (thus higher efficiency overall). This design philosophy has actually been applied by (Vorus & Mitchell 1994).
- The new design may lead to midchord cavitation (due to the very thin cavities especially towards the outer radii) and this will increase its frictional drag, and degrade somewhat the expected higher efficiency.

This case, and some more shown in (Kosal 1999), demonstrate that that *CAVOPT-3D* can obtain blade geometries with higher values of efficiency when compared to geometries designed with other methods.

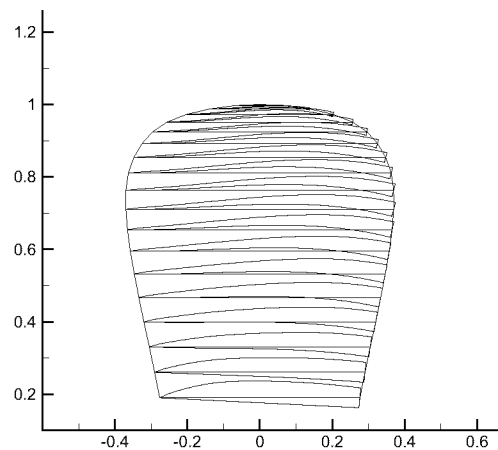


Figure 48: Blade contour and cross-sections of SRI/SSPA propeller.

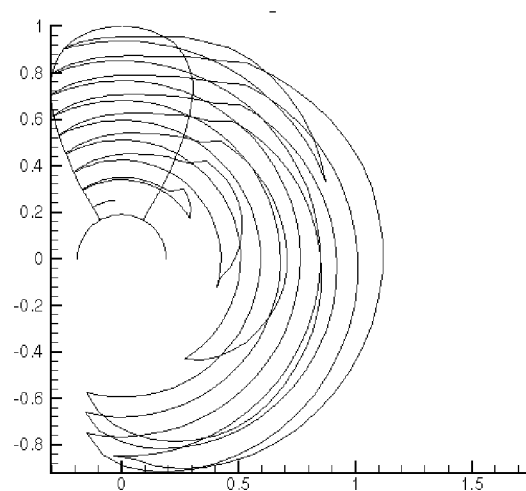


Figure 49: Cavity plan-form for SRI propeller; $J_S = 1.1$, $\sigma_n = 0.484$.

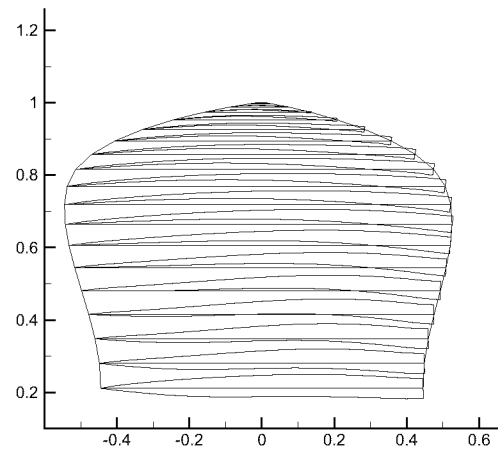


Figure 50: Blade contour and cross-sections of propeller design by CAVOPT-3D.

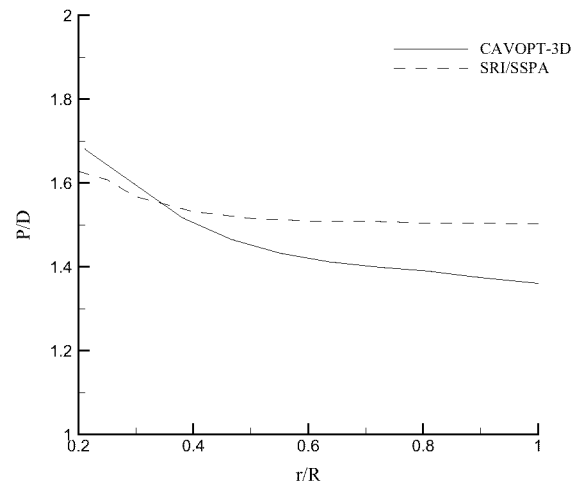


Figure 51: Pitch distributions for SRI/SSPA and CAVOPT-3D designs.

REFERENCES

- ABBOTT, I. AND VON DOENHOFF, A. 1959 *Theory of Wing Sections*. Dover, New York.
- ACHKINADZE, A. AND FRIDMAN, G. 1994 Artificial variation problems method for three-dimensional lifting cavity flows. *Proceedings: Twentieth Symposium on Naval Hydrodynamics*. August, 466–476.
- BAL, S., KINNAS, S. AND LEE, H. 2001 Numerical analysis of 2-D and 3-D cavitating hydrofoils under a free surface. *Journal of Ship Research*, **45**, 1, March, 34–49.
- BIRKHOFF, G. AND ZARANTONELLO, E. 1957 *Jets, Wakes and Cavities*. Academic Press Inc., New York.
- BRESLIN, J., VAN HOUTEN, R., KERWIN, J. AND JOHNSON, C.-A. 1982 Theoretical and experimental propeller-induced hull pressures arising from intermittent blade cavitation, loading, and thickness. *Trans. SNAME*, **90**.
- CHOI, J.-K. AND KINNAS, S. 1998 Numerical water tunnel in two and three dimensions. *Journal of Ship Research*, **42**, 2, June, pp. 86–98.
- CHOI, J.-K. AND KINNAS, S. 1999 Numerical model of a cavitating propeller inside of a tunnel. *Journal of Fluids Engineering*, **121**, June, 297–304.
- CHOI, J.-K. AND KINNAS, S. 2001 Prediction of non-axisymmetric effective wake by a 3-D Euler solver. *Journal of Ship Research*, **45**, 1, March, 13–33.
- CHOI, J. 2000 Vortical inflow – propeller interaction using unsteady three-dimensional euler solver. Doctoral dissertation, Department of Civil Engineering, The University of Texas at Austin. August.
- COMSTOCK, J., Ed. 1967 *Principles of Naval Architecture*. Society of Naval Architects and Marine Engineers.
- DESHPANDE, M., FENG, J. AND MERKLE, C. 1993 Navier-stokes analysis of 2-d cavity flow. *Proceedings: Cavitation and Multiphase Flow Forum*. FED-154, ASME, 149–155.
- DRELA, M. 1989 Integral boundary layer formulation for blunt trailing edges. *AIAA paper*, **89-2200**.
- FABULA, A. 1962 Thin-airfoil theory applied to hydrofoils with a single finite cavity and arbitrary free streamline detachment. *Journal of Fluid Mechanics*, **vol 12**, pp 227–240.
- FINE, N. E. 1992 Nonlinear analysis of cavitating propellers in nonuniform flow. Doctoral dissertation, Department of Ocean Engineering, MIT. October.
- FINE, N. AND KINNAS, S. 1993a A boundary element method for the analysis of the flow around 3-d cavitating hydrofoils. *Journal of Ship Research*, **37**, September, 213–224.
- FINE, N. AND KINNAS, S. 1993b The nonlinear numerical prediction of unsteady sheet cavitation for propellers of extreme geometry. *Proceedings: Sixth International Conference On Numerical Ship Hydrodynamics*. August, 531–544.
- FURUYA, O. 1975a Nonlinear calculation of arbitrarily shaped supercavitating hydrofoils near a free surface. *Journal of Fluid Mechanics*, **vol. 68**, pp 21–40.
- FURUYA, O. 1975b Three-dimensional theory on supercavitating hydrofoils near a free surface. *Journal of Fluid Mechanics*, **71**, pp. 339–359.
- GEURST, J. 1960 Linearized theory for fully cavitating hydrofoils. *International Shipbuilding Progress*, **vol 7**, No. 65, January.
- GRIFFIN, P. 1998 Computational techniques for the design and analysis of cavitating propeller blades. Masters thesis, UT Austin, Dept. of Civil Engineering. May.
- GRIFFIN, P. AND KINNAS, S. 1998 A design method for high-speed propulsor blades. *Journal of Fluids Engineering*, **120**, September, 556–562.
- HANAOKA, T. 1964 Linearized theory of cavity flow past a hydrofoil of arbitrary shape. *Journal of the Society of Naval Architects, Japan*, **vol. 115**, June, pp. 56–74.
- HUFFORD, G., DRELA, M. AND KERWIN, J. 1994 Viscous flow around marine propellers using boundary-layer strip theory. *Journal of Ship Research*, **38**, 1, March, pp. 52–62.
- ISHII, N. 1992 Prediction of propeller performance and cavitation based on the numerical modeling of propeller vortex system. *Proceedings: International Symposium on Propulsors and Cavitation*. pp. 33–41.

- JIANG, C. AND LEEHEY, P. 1977 A numerical method for determining forces and moments on supercavitating hydrofoils of finite span. *Proceedings: Second Int'l Conf. Numer. Ship Hydrodynamics*. September.
- KATO, H. 1994 Recent advances in cavitating foil research. *Proceedings: International Conference on Hydrodynamics*. pp. 80–89.
- KATO, H. 1996 *Cavitation*. Computational Mechanics Publications. in *Advances in Marine Hydrodynamics*. Chap. 5, pp 233–277.
- KERWIN, J., KINNAS, S., WILSON, M. AND MCHUGH, J. 1986 Experimental and analytical techniques for the study of unsteady propeller sheet cavitation. *Proceedings: Proceedings of the Sixteenth Symposium on Naval Hydrodynamics*. July, 387–414.
- KIM, Y.-G. AND LEE, C.-S. 1996 Prediction of unsteady performance of marine propellers with cavitation using surface-panel method. *Proceedings: 21st Symposium on Naval Hydrodynamics*. June.
- KIM, Y.-G., LEE, C.-S. AND SUH, J.-C. 1994 Surface panel method for prediction of flow around a 3-d steady or unsteady cavitating hydrofoil. *Proceedings: Second International Symposium on Cavitation*. April 5-7, 113–120.
- KINNAS, S. 1985 Non-linear corrections to the linear theory for the prediction of the cavitating flow around hydrofoils. Doctoral dissertation, Department of Ocean Engineering, MIT. May.
- KINNAS, S. 1991 Leading-edge corrections to the linear theory of partially cavitating hydrofoils. *Journal of Ship Research*, **35**, 1, March, pp. 15–27.
- KINNAS, S. 1992a Inversion of the source and vorticity equations for supercavitating hydrofoils. *Journal of Engineering Mathematics*, **26**, 349–361.
- KINNAS, S. 1992b Leading edge correction to the linear theory of cavitating hydrofoils and propellers. *Proceedings: Second International Symposium on Propeller and Cavitation*. September.
- KINNAS, S. 1998 Prediction of unsteady sheet cavitation. *Proceedings: Third International Symposium on Cavitation*. April 7-10, 19–36.
- KINNAS, S. AND FINE, N. 1991a Analysis of the flow around supercavitating hydrofoils with midchord and face cavity detachment. *Journal of Ship Research*, **35**, 3, September, pp. 198–209.
- KINNAS, S. AND FINE, N. 1991b Non-Linear Analysis of the Flow Around Partially or Super-Cavitating Hydrofoils by a Potential Based Panel Method. *Proceedings: Boundary Integral Methods-Theory and Applications*, Proceedings of the IABEM-90 Symposium, Rome, Italy, October 15-19, 1990. Springer-Verlag, Heidelberg, 289–300.
- KINNAS, S. AND FINE, N. 1992 A nonlinear boundary element method for the analysis of unsteady propeller sheet cavitation. *Proceedings: Nineteenth Symposium on Naval Hydrodynamics*. August, 717–737.
- KINNAS, S. AND FINE, N. 1993 A numerical nonlinear analysis of the flow around two- and three-dimensional partially cavitating hydrofoils. *Journal of Fluid Mechanics*, **254**, September, 151–181.
- KINNAS, S. AND HSIN, C.-Y. 1992 A boundary element method for the analysis of the unsteady flow around extreme propeller geometries. *AIAA Journal*, **30**, 3, March, 688–696.
- KINNAS, S. AND MAZEL, C. 1992 Numerical vs. experimental cavitation tunnel (a supercavitating hydrofoil experiment). *Proceedings: 23rd American Towing Tank Conference*. June 11-12.
- KINNAS, S., MISHIMA, S. AND BREWER, W. 1994 Nonlinear analysis of viscous flow around cavitating hydrofoils. *Proceedings: Twentieth Symposium on Naval Hydrodynamics*. August, 446–465.
- KINNAS, S., MISHIMA, S. AND SAVINEAU, C. 1995 Application of optimization techniques to the design of cavitating hydrofoils and wings. *Proceedings: CAV'95 International Symposium on Cavitation*. May 2-5, 135–143.
- KINNAS, S., GRIFFIN, P., CHOI, J.-K. AND KOSAL, E. 1998a Automated design of propulsor blades for high-speed ocean vehicle applications. *Trans. SNAME*, **106**.
- KINNAS, S., LEE, H. AND MUELLER, A. 1998b Prediction of propeller blade sheet and developed tip vortex cavitation. *Proceedings: 22nd Symposium on Naval Hydrodynamics*. August 9-14, 182–198.
- KINNAS, S., KOSAL, E. AND YOUNG, J. 1999a Computational techniques for the design and analysis of super-cavitating propellers. *Proceedings: FAST'99 - 5th International Conference on Fast Sea Transportation*. August 31-September 2.

KINNAS, S., CHOI, J.-K., KOSAL, E., YOUNG, J. AND LEE, H. 1999b An integrated computational technique for the design of propellers with specified constraints on cavitation extent and hull pressure fluctuations. *Proceedings: CFD99 - The International CFD Conference*. June 5-7.

KINNAS, S., CHOI, J., LEE, H. AND YOUNG, J. 2000 Numerical Cavitation Tunnel. *Proceedings: NCT'50, International Conference on Propeller Cavitation*. April 3-5, 137-157.

KOSAL, E. 1999 Improvements and enhancements in the numerical analysis and design of cavitating propeller blades. Masters thesis, UT Austin, Dept. of Civil Engineering. May. Also, UT Ocean Eng. Report 99-1.

KRISHNASWAMY, P. 1999 Re-entrant jet and viscous flow modeling for partially cavitating hydrofoils. Technical report. No. 99-3. Ocean Eng. Group, Department of Civil Engineering, UT Austin. June.

KUBOTA, A., KATO, H. AND YAMAGUCHI, H. 1989 Finite difference analysis of unsteady cavitation on a two-dimensional hydrofoil. *Proceedings: Fifth International Conference on Numerical Ship Hydrodynamics*. September, 667-683.

KUDO, T. AND UKON, Y. 1994 Calculation of supercavitating propeller performance using a vortex-lattice method. *Proceedings: Second International Symposium on Cavitation*. April 5-7, 403-408.

LEE, C.-S. 1979 Prediction of steady and unsteady performance of marine propellers with or without cavitation by numerical lifting surface theory. Doctoral dissertation, M.I.T., Department of Ocean Engineering. May.

LEE, C.-S. 1981 Prediction of the transient cavitation on marine propellers. *Proceedings: Thirteenth Symposium on Naval Hydrodynamics*. 41-64.

LEE, C.-S., KIM, Y.-G. AND LEE, J.-T. 1992 A potential-based panel method for the analysis of a two-dimensional super- or partially- cavitating hydrofoil. *Journal of Ship Research*, **36**, 2, March, pp. 168-181.

LEEHEY, P. 1971 Supercavitating hydrofoil of finite span. *Proceedings: IUTAM Symposium on Non-Steady Flow of Water at High Speeds*. June, 277-298.

LEMONNIER, H. AND ROWE, A. 1988 Another approach in modelling cavitating flows. *Journal of Fluid Mechanics*, vol **195**.

MATSUDA, N., KUROBE, Y., UKON, Y. AND KUDO, T. 1994 Experimental investigation into the performance of supercavitating propellers. *Papers of Ship Research Institute*, **31**, 5.

MISHIMA, S. 1996 Design of cavitating propeller blades in non-uniform flow by numerical optimization. Doctoral dissertation, M.I.T., Department of Ocean Engineering. September.

MISHIMA, S. AND KINNAS, S. 1996 A numerical optimization technique applied to the design of two-dimensional cavitating hydrofoil sections. *Journal of Ship Research*, **40**, 1, March, pp. 28-38.

MISHIMA, S. AND KINNAS, S. 1997 Application of a numerical optimization technique to the design of cavitating propellers in non-uniform flow. *Journal of Ship Research*, **41**, 2, June, pp. 93-107.

MORINO, L. AND KUO, C.-C. 1974 Subsonic Potential Aerodynamic for Complex Configurations : A General Theory. *AIAA Journal*, vol **12**, no 2, February, pp 191-197.

MUELLER, A. 1998 Development of face and mid-chord cavitation models for the prediction of unsteady cavitation on a propeller. Masters thesis, UT Austin, Dept. of Civil Engineering. May.

MUELLER, A. AND KINNAS, S. 1999 Propeller sheet cavitation predictions using a panel method. *Journal of Fluids Engineering*, **121**, June, 282-288.

MUSKHELISHVILI, N. I. 1946 *Singular Integral Equations*. P. Noordhoff, Limited, Groningen, Holland.

NISHIYAMA, T. 1970 Lifting line theory of supercavitating hydrofoil of finite span. *ZAMM*, **50**, 645-653.

OHBA, R. 1963/1964 Theory on supercavitating hydrofoils at arbitrary cavitation coefficients. Technical report. Vol. 15. Institute of High Speed Mechanics, Tohoku University.

OLOFSSON, N. 1996 Force and flow characteristics of a partially submerged propeller. Doctoral dissertation, Department of Naval Architecture and Ocean Engineering, Chalmers University of Technology, Göteborg, Sweden. February.

PELLONE, C. AND PEALLAT, J. 1995 Non-linear analysis of three-dimensional partially cavitating hydrofoil. *Proceedings: CAV'95 International Symposium on Cavitation*. May 2-5, 433-440.

- PELLONE, C. AND ROWE, A. 1981 Supercavitating hydrofoils in non-linear theory. *Proceedings: Third International Conference on Numerical Ship Hydrodynamics*. Basin d'essais des Carènes, Paris, France, June.
- ROWE, A. AND BLOTTIAUX, O. 1993 Aspects of modeling partially cavitating hydrofoils. *Journal of Ship Research*, **37**, 1, pp. 34–48.
- RUTGERSSON, O. 1979 Supercavitating propeller performance. SSPA Publication No. 82, Goteborg, Sweden.
- SHIBA, H. 1953 Air-drawing of marine propellers. Technical report. 9. Transportation Technical Research Institute. August.
- STERN, F. AND VORUS, W. 1983 A nonlinear method for predicting unsteady sheet cavitation on marine propellers. *Journal of Ship Research*, **38**, 1, pp. 56–74.
- SZANTYR, J. 1994 A method for analysis of cavitating marine propellers in non-uniform flow. *International Shipbuilding Progress*, **41**, pp. 223–242.
- TULIN, M. 1953 Steady two-dimensional cavity flows about slender bodies. Technical report. 834. DTMB. May.
- TULIN, M. 1964 Supercavitating flows - small perturbation theory. *Journal of Ship Research*, **vol 7**, No. 3, pp. 16–37.
- TULIN, M. AND HSU, C. 1980 New applications of cavity flow theory. *Proceedings: 13th Symposium on Naval Hydrodynamics*.
- UHLMAN, J. 1978 A partially cavitated hydrofoil of finite span. *Journal of Fluids Engineering*, **100**, 3, September, pp. 353–354.
- UHLMAN, J. 1987 The surface singularity method applied to partially cavitating hydrofoils. *Journal of Ship Research*, **vol 31**, No. 2, June, pp. 107–124.
- UHLMAN, J. 1989 The surface singularity or boundary integral method applied to supercavitating hydrofoils. *Journal of Ship Research*, **vol 33**, No. 1, March, pp. 16–20.
- VAN GENT, W. 1994 Pressure field analysis of a propeller with unsteady loading and sheet cavitation. *Proceedings: Twentieth Symposium on Naval Hydrodynamics*. August, 355–367.
- VAN HOUTEN, R. 1982 The numerical prediction of unsteady sheet cavitation on high aspect ratio hydrofoils. *Proceedings: 14th Symposium on Naval Hydrodynamics*.
- VORUS, W. AND MITCHELL, K. 1994 Engineering of power boat propellers. *Proceedings: Propellers/Shafting '94 Symposium*. Society of Naval Architects & Marine Engineers, Virginia Beach, VA, September 20–21, 1–16 (paper No. 12).
- WIDNALL, S. 1966 Unsteady loads on supercavitating hydrofoils. *Journal of Ship Research*, **9**, pp. 107–118.
- WU, T. 1957 A simple method for calculating the drag in the linear theory of cavity flows. Technical report. No. 85-5. California Institute of Technology, Hydrodynamics Laboratory. August.
- WU, T. AND WANG, D. 1964 A wake model for free-streamline flow theory. part 2. cavity flows past obstacles of arbitrary profile. *Journal of Fluid Mechanics*, **vol 18**, pp 65–93.
- YAMAGUCHI, H. AND KATO, H. 1983 On application of nonlinear cavity flow theory to thick foil sections. *Proceedings: Second International Conference on Cavitation*. IMechE, 167–174.
- YIM, B. 1974 Linear theory on water entry and exit problems of a ventilating thin wedge. *Journal of Ship Research*, **18**, 1, pp. 1–11.
- YOUNG, Y. AND KINNAS, S. 2000 Prediction of unsteady performance of surface-piercing propellers. *Proceedings: Propellers/Shafting 2000 Symposium*. Soc. Naval Arch. & Marine Engrs., Virginia Beach, VA, September 20–21, 1–9 (paper No. 7).
- YOUNG, Y. AND KINNAS, S. 2001 A BEM for the Prediction of Unsteady Midchord Face and/or Back Propeller Cavitation. *Journal of Fluids Engineering*, **123**, June. to appear.
- YOUNG, Y., LEE, H. AND KINNAS, S. 2001 PROPCAV (version 1.2) user's manual and documentation. Technical report. No. 01-4. Ocean Engineering Group, UT Austin. January.

CAVOPT-3D (v 1.3) OUTPUT

mid28

Design Conditions

$$\begin{aligned} J_s &= 1.100 \\ \sigma_n &= 0.484 \\ F_n &= 5.000 \\ \text{NBLADE} &= 3. \\ r_H/R &= 0.190 \\ K_{To} &= 0.1750 \end{aligned}$$

Design Constraints

PTOL = -0.100

Design Parameters

Chord Optimized
Skew Fixed (Skew from *.geo file)

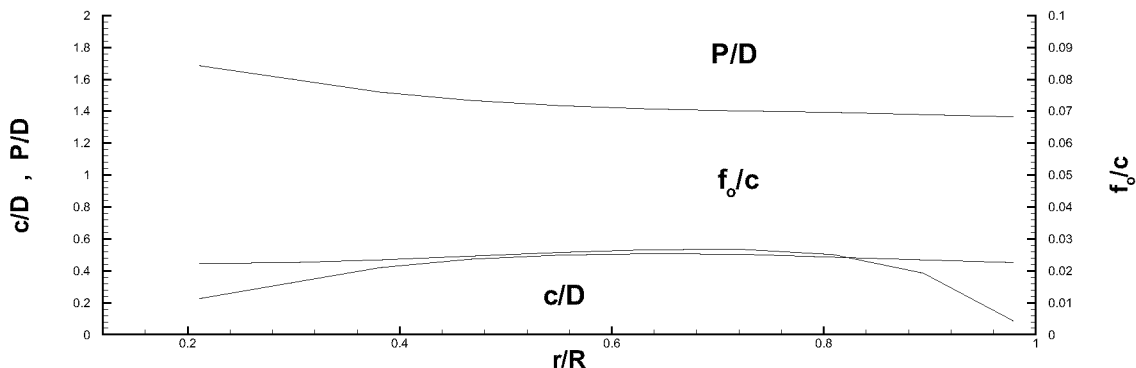
MPUF-3A Parameters

MPUF-3A MIDCHORD/TIP/HUB/PROP CAVITATING SEPTEMBER 98 EDITION

```
PROPELLER INPUT GEOMETRY FILE: sspall !geometry filename, wi.GEO
Header: -- Surface Piercing, Super-Cavitating Cross Section 11 radii (except 0
WAKE INPUT FILE: uniform !wake filename, withou.WAK
Header: SAMPLE WAKE FOR CAVOPT3D
NPROP= 1 IAXIS= 1 MXREV= 5 NFCN= 1 NN= 20
IHUB= 0 ILEON= 0 NX= 11 MCAM= 1 MTHK= 1 NBLADE= 3 IALIGN= 2
MM= 9 SJ= 1.1000 SIGMAN= 0.4840 FROUDE= 5.0000
```

Final Design

$\eta = 0.7468$	Blade Angle at Max Cavity Volume = 150°	Max Back Cav Area/Blade Area = 1.2705
$K_Q = 0.0409$	Max Cavity Vol/ $R^3 = 0.04588$	Max Face Cav Area/Blade Area = 0.0000
$K_r = 0.1746$	CVV = 0.08570	DPV = -0.06493



Convergence History

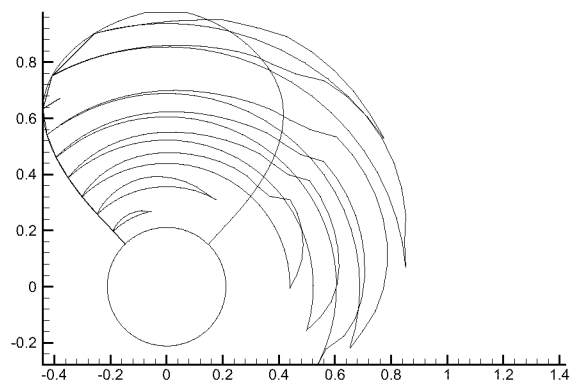
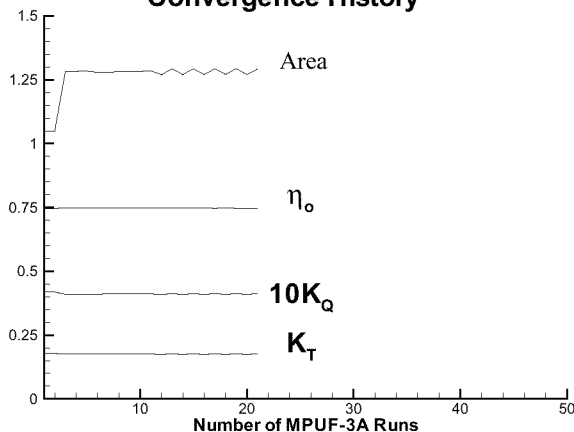


Figure 52: *CAVOPT-3D* design summary sheet. Note that this has been a quadratic run, i.e. a run that used the history of a previous run in which $PTOL = -0.3$.